The Astrophysical Journal, 597:535–554, 2003 November 1

MULTIWAVELENGTH OBSERVATIONS OF FLARES ON AD LEONIS

Suzanne L. Hawley,[1,2] Joel C. Allred,[1,2] Christopher M. Johns-Krull,[2,3] George H. Fisher,[2,4] William P. Abbett,[2,4] Ilya Alekseev,[5,6] Stavros I. Avgoloupis,[7] Susana E. Deustua,[8] Alastair Gunn,[9] John H. Seiradakis,[7] Martin M. Sirk,[4] and Jeff A. Valenti[10]

Received 2003 May 6; accepted 2003 July 9

ABSTRACT

We report results from a multiwavelength observing campaign conducted during 2000 March on the flare star AD Leo. Simultaneous data were obtained from several ground- and space-based observatories, including observations of eight sizable flares. We discuss the correlation of line and continuum emission in the optical and ultraviolet wavelength regimes, as well as the flare energy budget, and we find that the emission properties are remarkably similar even for flares of very different evolutionary morphology. This suggests a common heating mechanism and atmospheric structure that are independent of the detailed evolution of individual flares. We also discuss the Neupert effect, chromospheric line broadening, and velocity fields observed in several transition region emission lines. The latter show significant downflows during and shortly after the flare impulsive phase. Our observations are broadly consistent with the solar model of chromospheric evaporation and condensation following impulsive heating by a flux of nonthermal electrons. These data place strong constraints on the next generation of radiative hydrodynamic models of stellar flares.

Subject headings: stars: chromospheres — stars: flare — stars: individual (AD Leonis) — stars: low-mass, brown dwarfs

1. INTRODUCTION

Flares are by their nature random and unpredictable events, and flare observations are often the serendipitous result of observations designed for other scientific endeavors (Joy & Humason 1949; Herbig 1956; Pettersen et al. 1990; Liebert et al. 1999). While these observations are useful for finding new flare stars and for their initial characterization, the investigation of detailed flare physics demands simultaneous observations in multiple wavelength regimes, with both spectroscopic and photometric information. Our recent advances in flare modeling (Abbett & Hawley 1999), together with the availability of a new generation of space instrumentation offering order-of-magnitude improvement in time resolution (*Far Ultraviolet Spectroscopic Explorer* [*FUSE*], *Hubble Space Telescope*/Space Telescope Imaging Spectrograph [*HST*/STIS]), led us to organize a large flare campaign on the bright, well-known dM3e flare star AD Leonis during 2000 March.

AD Leo is one of the most active single M dwarfs in the northern hemisphere and has been observed extensively by ourselves and others (Rodono et al. 1989; Hawley & Pettersen 1991; Bookbinder, Walter, & Brown 1992; Hawley et al. 1995; Mauas & Falchi 1996; Cully et al. 1997). In many aspects, flares on AD Leo resemble those on the Sun, including the appearance of impulsive continuum emission and longer-lived soft X-rays and chromospheric emission lines. These are explained in the canonical solar model as a manifestation of chromospheric evaporation during the initial flare energy release and are empirically connected through the Neupert effect, observed in some 80% of large solar flares (Dennis & Zarro 1993; McTiernan et al. 1999). The Neupert effect has been observed on AD Leo in optical, soft X-ray, and radio emission (Hawley et al. 1995; Güdel et al. 1996). Stark broadening has also been reported in the Balmer series lines in both solar and stellar flares (Donati-Falchi et al. 1985; Hawley & Pettersen 1991; Johns-Krull et al. 1997). However, while velocity shifts indicating large-scale mass motions are often observed in solar flares, the stellar data are ambiguous and generally of too poor a quality for meaningful interpretation. The behavior of ultraviolet emission lines is also relatively unexplored in flare stars, although we have previously predicted from theoretical considerations that these may provide an important source of heating during the gradual phase of a flare (Hawley & Fisher 1992). Finally, our recent work on solar flare models incorporating radiative hydrodynamics (Abbett & Hawley 1999) and our plans to extend these models to the stellar flare regime demand constraints on velocity fields and emission timescales for numerous species over a wide range of temperature. New data with high time and spectral resolution are therefore required.

The campaign was planned to include the *FUSE*, *HST*, and *EUVE* (*Extreme Ultraviolet Explorer*) satellites, ground-based optical telescopes at the McDonald Observatory, the Dominion Astrophysical Observatory (DAO), the

[1] University of Washington, Department of Astronomy, Box 351580, Seattle, WA 98195.
[2] Kavli Institute for Theoretical Physics, University of California, Santa Barbara, CA 93106.
[3] Department of Physics and Astronomy, 6100 Main Street, Rice University, Houston, TX 77005.
[4] Space Sciences Laboratory, University of California, Berkeley, CA 94720.
[5] Crimean Astrophysical Observatory, Nauchny, Crimea 98409, Ukraine.
[6] Isaac Newton Institute of Chile, Crimean branch.
[7] Aristotle University of Thessaloniki, Department of Physics, Section of Astrophysics, Astronomy, and Mechanics, GR-54124 Thessaloniki, Greece.
[8] American Astronomical Society, 2000 Florida Avenue, NW, Suite 400, Washington, DC 20009.
[9] University of Manchester, Jodrell Bank Observatory, Macclesfield, Cheshire SK11 9DL, UK.
[10] Space Telescope Science Institute, 3700 San Martin Drive, Baltimore, MD 21218.

Stephanion Observatory, and the Crimean Astrophysical Observatory (CrAO), and the MERLIN array operated by the Jodrell Bank Observatory. Unfortunately, the *FUSE* satellite went into safe mode just hours before the scheduled start of our observation, and no data were obtained. The DAO and CrAO facilities were plagued with poor weather. Their monitoring data were useful to show that no very large flares occurred during the periods they were observing but could not be used in a quantitative fashion. The radio data from Jodrell Bank indicated no firm detection of the source. The other telescopes recorded excellent data, encompassing several energetic flares, and we report on those results here.

Section 2 contains a description of the telescopes and instruments, the types of data obtained, and the data reduction procedures. Section 3 describes our observation of the stellar Neupert effect in soft X-rays and *U*-band radiation. Section 4 gives our results on the optical and ultraviolet continuum and line radiation, including discussion of the flare energy budgets, line broadening, and velocity fields. Finally, in § 5 we present our preliminary conclusions and plans for future work incorporating these data.

2. OBSERVATIONS

Figure 1 shows an overview of the data obtained during the 2000 March AD Leo flare campaign, and Table 1 lists the observing times, instruments, and observers who participated. At the top of the figure, we have indicated the eight substantial flares that were observed. The final data products discussed here include *U*-band photometry from the Stephanion Observatory (flares 1, 2, and 5), *UBVR* photometry from the McDonald Observatory 2.1 m telescope (flares 3, 6, 7, and 8), coudé spectroscopy with resolution 55,000 from the McDonald Observatory 2.7 m telescope (flares 3, 6, 7, and 8), soft X-ray photometry and spectroscopy from the NASA *EUVE* satellite Deep Survey (DS) and spectrometer instruments (spanning flares 1 and 2), and ultraviolet spectroscopy with resolution 70,000 from the *HST* using STIS (flares 3, 4, 6, 7, and 8). The following sections describe each of these data sources in detail.

2.1. *Stephanion Observatory Photometry*

Photoelectric photometry through a Johnson *U* filter was carried out at the Stephanion Observatory with the University of Thessaloniki 30 inch (0.76 m) Cassegrain reflecting telescope. The telescope, instrument, and observing procedure are described in Mavridis et al. (1982). The observations consisted of continuous monitoring of AD Leo at a cadence of 0.1 s, with brief excursions to measure sky brightness. Comparison stars were observed periodically. The data were reduced to instrumental intensities and magnitudes, and the magnitude of the quiescent state of AD Leo was matched to the reference provided by overlapping observations at McDonald Observatory (see below). The weather was only partially clear during the three nights of monitoring, resulting in a total of 6.2 hr of usable data. The largest optical flare during the campaign was observed simultaneously by Stephanion and *EUVE* and is discussed in § 3.

2.2. *McDonald Observatory Photometry*

Photoelectric photometry in the Johnson *UBVR* filters was obtained with the McDonald Observatory 2.1 m Struve

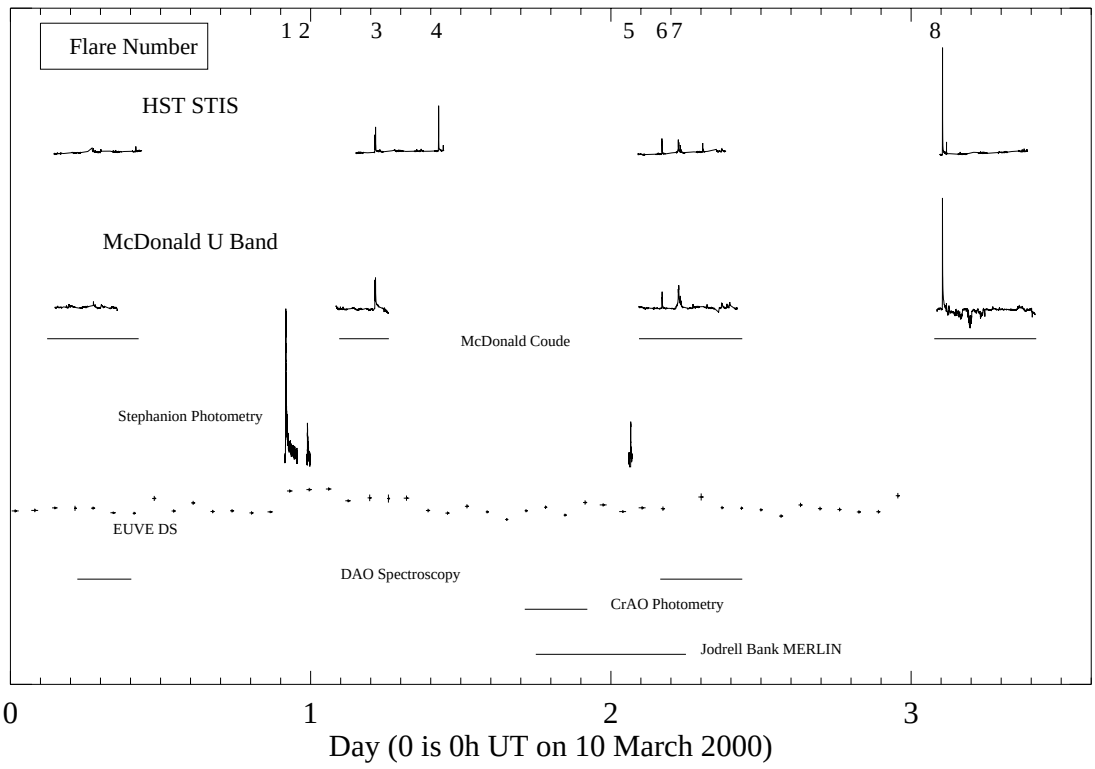

FIG. 1.—Observation periods are shown for the instruments that were involved in the AD Leo flare campaign. The time is in days from 00 UT on 2000 March 10. Light curves (in normalized units) are given for the STIS, *EUVE*, McDonald *U*-band, and Stephanion photometry fluxes only. The eight flares analyzed in this paper are indicated by number along the top of the figure.

TABLE 1
OBSERVING LOG

Telescope/Instrument	Observer	Time[a] (UT)	Wavelength/Resolution
HST/STIS	Valenti	10d: 3:28–10:30; 11d: 3:36–10:38; 12d: 2:09–9:10; 13d: 2:17–9:18	1160–1700 Å, $R = 70,000$
McDonald 2.1 m photometer	Johns-Krull	10d: 3:33–10:21; 11d: 2:00–6:13; 12d: 2:12–11:03; 13d: 2:03–9:55	*U*, *B*, *V*, *R*
McDonald 2.7 m coudé spectrograph	Hawley	10d: 2:56–10:15; 11d: 2:17–6:15; 12d: 2:15–10:30; 13d: 1:51–10:00	3800–8800 Å, $R = 55,000$
Stephanion 30 inch photometer	Seiradakis & Avgoloupis	10d: 20:58–25:53; 11d: 23:53–26:41	*U*
EUVE Deep Survey/Spectrometer	Fisher	9d: 13:34– 12d: 23:17	60–190 Å/$R = 200$
DAO 72 in (1.8 m) spectrometer	Abbett & Deustua	10d: 5:21–9:40; 12d: 3:57–10:30	3500–7000 Å
CrAO 1.25 m photometer	Alekseev	11d: 17:07–22:07	*UBVRI*
Jodrell Bank/MERLIN	Gunn	11d: 18:00–12d 6:00	5 GHz

[a] 10d is 2000 March 10; 11d is 2000 March 11, etc.

telescope equipped with a two-channel photometer. AD Leo was observed with the primary channel, while the second channel monitored the sky conditions. Integrations of 0.8 s in each filter, combined with 0.2 s for filter rotation, resulted in a 4 s cycle time. Sky measurements were made in the primary channel every 15–20 minutes. Extinction and photometric standard stars (Landolt 1973, 1992) were observed each night, and the data were reduced to magnitudes and colors in the standard *UBVR* system. The absolute photometric accuracy, based on our standard star observations and our previous experience with this instrument (Hawley & Pettersen 1991; Hawley et al. 1995), is approximately ± 0.02 mag. The internal precision (i.e., measured from the Poisson statistics of the count rates) is even better, being ~ 0.01 mag in *U* and a few millimagnitudes in *B*, *V*, and *R* (the result of observing a ninth-magnitude star photometrically with an 82 inch [2.1 m] telescope!).

The weather was quite good at McDonald, resulting in the loss of only a half-night of observations during the four-night campaign, although clouds were evident during a few hours on the other nights. Figure 1 shows the light curves for the four nights of observations. Four large flares are marked (flares 3, 6, 7, and 8); there were also numerous smaller flares that we are still in the process of analyzing.

2.3. *McDonald Observatory Spectroscopy*

We used the McDonald Observatory 2.7 m Harlan Smith telescope and the cross-dispersed coudé echelle spectrograph (Tull et al. 1995) to obtain high-resolution optical spectroscopy with a time resolution of 70 s (20 s exposures followed by 50 s for readout and writing to disk). The wavelength range was nominally 3800–8800 Å, with small gaps between each of the 61 orders except in the far blue. Because of the relative faintness of AD Leo in the blue and the short exposure times, the region blueward of Hδ was usually too noisy for reliable measurements. The data were recorded on a 2048×2048 Tektronix CCD that was binned 2×2 to decrease readout time. As a result of this binning, the detector undersampled the spectrum. Spectra of a thorium-argon lamp were used to determine the wavelength solution of the instrument and to measure the resolution obtained during the run. The median FWHM of the 1210 thorium lines used in the wavelength solution was 1.16 pixels, corresponding to a spectral resolution $R = 55,000$. The wavelength solution was determined by fitting a two-dimensional polynomial to $m\lambda$ as a function of detector column number and spectral order *m*. Spectra themselves were reduced in a standard way using software written in the IDL programing language and described by Hinkle et al. (2000). Briefly, the reductions include cosmic-ray removal, dark current and background subtraction, flat-fielding by a normalized exposure of an incandescent lamp, and extraction of the spectral orders using an optimal extraction algorithm. The optimal extraction algorithm is particularly effective at removing cosmic-ray defects, as discussed in Piskunov & Valenti (2002). The continuum was normalized in each echelle order, enabling measurement of equivalent widths and line profile parameters. Line fluxes were found using continuum measurements from a spectrophotometrically calibrated AD Leo spectrum observed by Pettersen & Hawley (1989). Spectra were analyzed for flares 3, 6, 7, and 8.

2.4. *EUVE Deep Survey Photometry*

AD Leo was observed for 294 ks (from HJD 2,451,613.06532 to HJD 2,451,616.47099) by the *EUVE* Deep Survey Imager and three spectrometers covering the short (SW: 100–250 Å), medium (MW: 250–500 Å), and long (LW: 500–700 Å) wavelength regions of the extreme-ultraviolet spectrum (Malina & Bowyer 1991; Siegmund et al. 1986). Background count rates were remarkably low in spite of increased airglow from the solar maximum. The satellite was carefully positioned to avoid the "dead spot," minimizing the uncertainty associated with that area of decreased sensitivity on the detector.

EUVE DS photometry was obtained through the Lexan-Boron filter (90% passband between 67 and 178 Å; Sirk et al. 1997). The DS light curve was created by defining a source region 13 pixels in radius and an annular background region with inner and outer radii of 50 and 100 pixels, respectively. Since the source region comprises only 2.2% of the area of the background region, the contribution to the Poisson error from the background subtraction is negligible. Time intervals where the total detector counts exceeded 1000 counts s^{-1} were excluded, as were intervals where the dead-time correction exceeded 200%. Approximately 15% of the DS data were rejected by these criteria. The mean count rate in the DS data was 0.23 counts s^{-1}, with a maximum of about 0.5 counts s^{-1} during the one flare observed. These correspond to observed fluxes of $\sim(3\text{–}6) \times 10^{-12}$ ergs cm^{-2} s^{-1}.

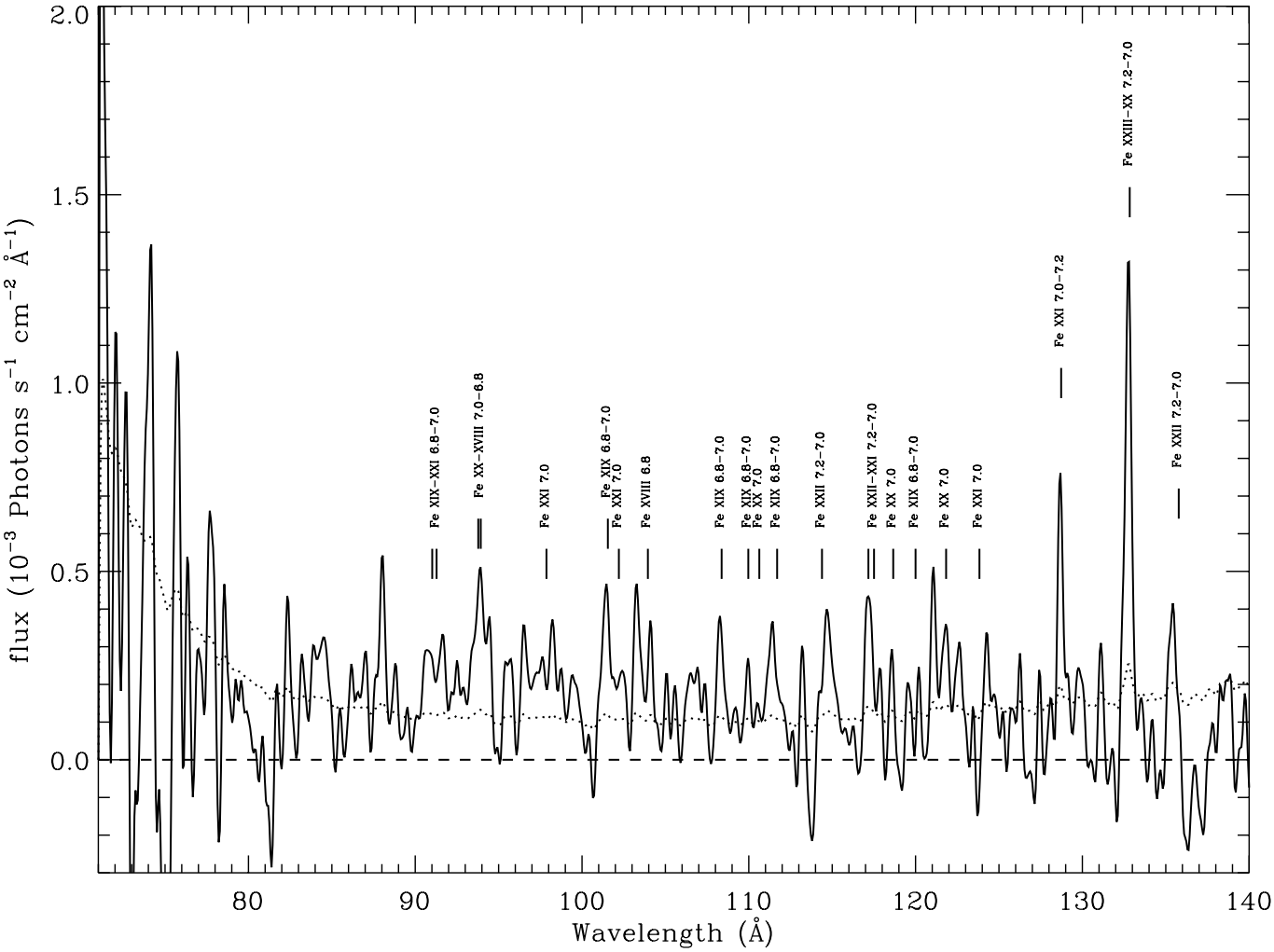

FIG. 2.—Spectrum obtained with the SW spectrometer on *EUVE*. The dotted line indicates the 1 σ error.

The spectra for the SW spectrometer were extracted as follows. First, time intervals were defined that excluded periods of high background (less than 2% of the time). Additional intervals were created corresponding to the quiet and flare periods of the DS light curve. The time filters were applied to the photon list, and images were created. A narrow strip of 13 pixels centered on the spectrum defined the spectral region, and two rectangular regions above and below the spectrum, each of 100 pixel extent, were used for background determination. The background spectrum was very noisy because of the low count rate. It was modeled following Hurwitz et al. (1997), so that no additional Poisson noise was added to the spectrum from the background estimate.

Figure 2 shows the SW spectrum obtained from the entire observation. There are $\sim$15 iron lines, indicative of plasma with temperatures between 5 and 20 million degrees. SW spectra extracted during the quiet and flare states appear different, but the low count rates preclude a more quantitative estimate. No measurable flux was seen in the MW or LW spectrometers.

2.5. *HST*/STIS Spectroscopy

The STIS instrument aboard *HST* was used with the FUV-MAMA detector in TIMETAG mode to obtain the highest possible time resolution. The E140M grating centered at 1425 Å, combined with the $0\farcs2 \times 0\farcs2$ aperture, results in a line-spread function with an FWHM of $\sim$1.3 pixels according to the STIS Instrument Handbook. This undersampled spectrum has resolution $R \sim 70,000$ over the wavelength range 1160–1700 Å. The data were processed in a customized way using software written in IDL in order to extract spectra in various time intervals. The time-tagged data files were used to identify the location on the detector of all photons recorded in a specified time interval. Spectra were then extracted from each order by summing all counts in each column that were detected within 7 pixels of the order locations returned by the *HST* archive. The background (generally negligible) was estimated by fitting a second-order polynomial to the background from either side of the order in question. Background spectra were constructed by extracting spectra centered between each order and summing the 3 pixels in each column around this location. The pipeline reduction flux calibration for converting count rate to flux was then applied to each spectrum to determine the observed flux. The flux calibration was checked by-extracting spectra for each of the five *HST* visits to AD Leo and comparing the results with the STIS pipeline reductions. On the basis of this comparison, we estimate the absolute flux calibration is accurate to $\sim$2%.

Uncertainties in the observed flux are determined from the Poisson statistics of the detected source counts and estimated background level. For weak lines and continua, the flux uncertainties are dominated by the Poisson statistics, not the flux calibration.

Five strong flares were observed with *HST*/STIS (flares 3, 4, 6, 7, and 8). Flare 4 occurred during a period of cloudy weather at McDonald Observatory, while the other four flares have simultaneous optical observations. Numerous smaller flares were also observed. Figure 3*a* shows the STIS

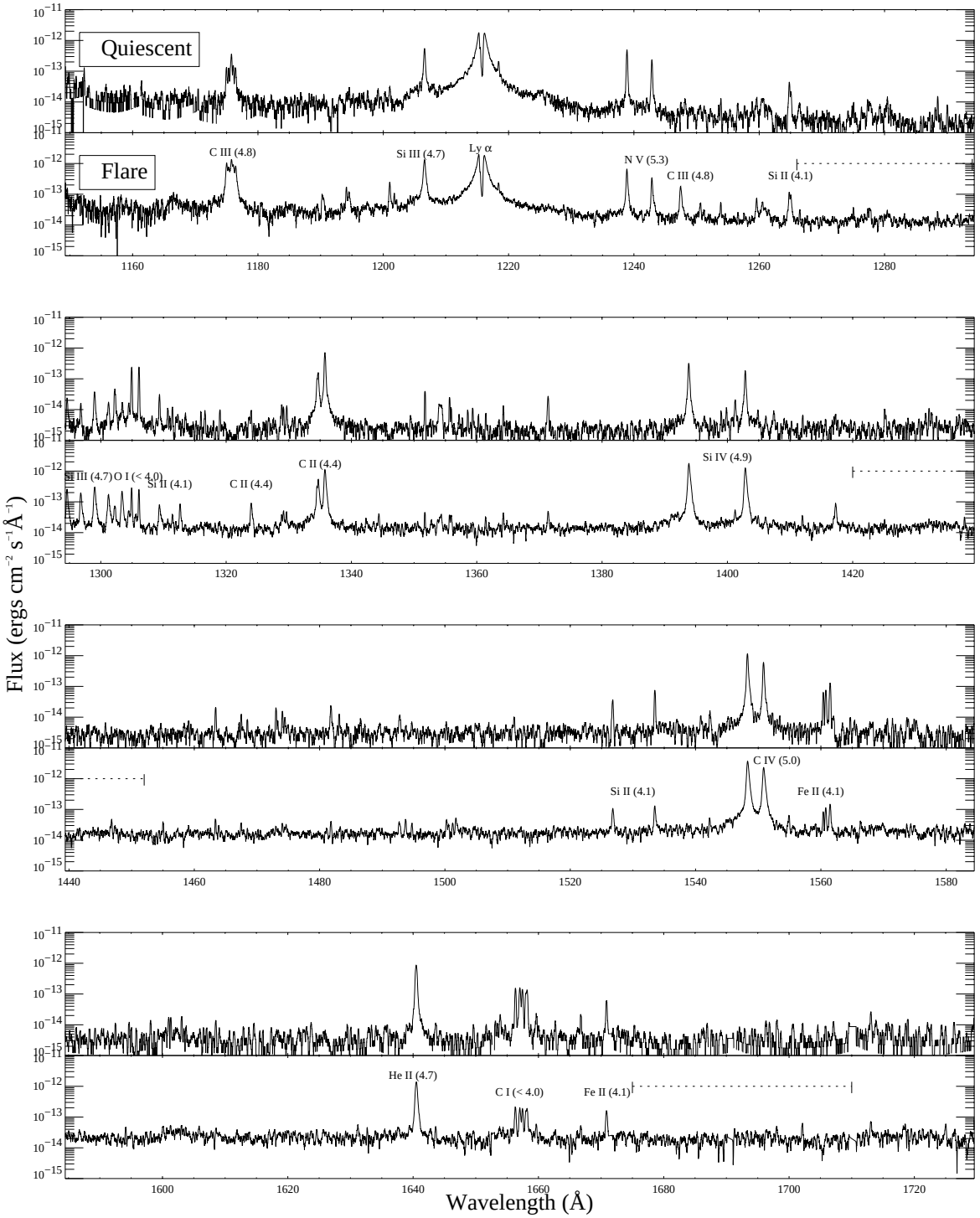

FIG. 3*a*

FIG. 3.—(*a*) Spectra obtained with *HST*/STIS during a period of quiescence (*top of each panel*) and during a sizable flare (*bottom of each panel*). The flaring spectrum consists of 3 minutes of data during flare 8, and the quiescent spectrum consists of 36 minutes of data obtained a day earlier. The dotted lines indicate the regions that were averaged together to measure the UV continuum. Numerous emission lines are identified, and the log of the formation temperature is indicated in parentheses next to each line. The spectra are plotted on a logarithmic flux scale to emphasize the enhanced continuum during the flare. (*b*) Flare enhancements in several strong emission lines used in our analysis on a linear flux scale for the same quiescent (*dotted line*) and flare (*solid line*) spectra shown in (*a*).

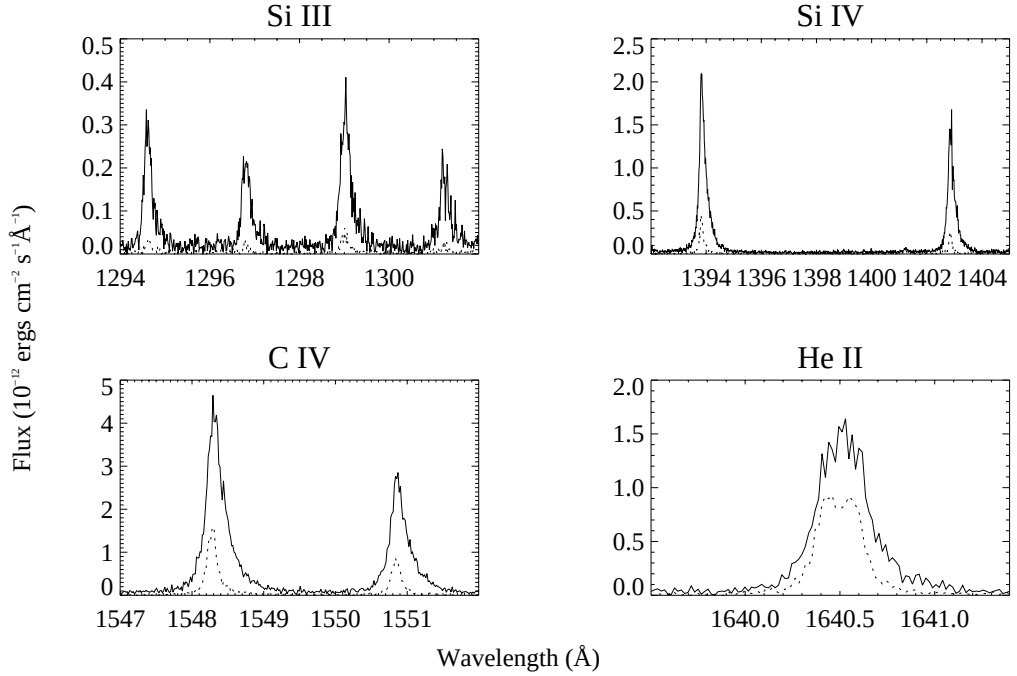

FIG. 3*b*

spectrum observed by extracting 36 minutes of quiescent data, together with the flare spectrum from 3 minutes around the peak of flare 8. The data are plotted on a logarithmic flux scale to emphasize the enhanced continuum emission during the flare. Figure 3*b* illustrates, on a linear flux scale, the response of the strong emission lines during the flare. Clearly there is a wealth of detailed information contained in this ultraviolet wavelength region.

For each of the large flares, we extracted the time-tagged data to obtain spectra with reasonable signal-to-noise ratio (S/N) while still preserving the best possible time resolution. Typically, the spectra used in our analysis represent 8–16 s integration times. We measured line fluxes and line-profile parameters directly from the extracted spectra and also defined continuum regions between the strong lines to obtain a measure of the ultraviolet continuum flux, as shown in Figure 3*a*.

2.6. *Summary*

The flare data described above divide naturally into two categories. The Stephanion optical photometry overlaps the only flare observed with *EUVE*, enabling us to further investigate the Neupert effect (§ 3). The McDonald optical photometry and spectroscopy overlap the STIS ultraviolet data, allowing us to examine in detail the line and continuum emission, energy budget, line broadening, and velocity fields. Data were obtained for several flares, allowing us to compare and contrast flares of varying strength and evolutionary morphology (§ 4).

3. THE NEUPERT EFFECT

During a solar flare, the time integral of the hard X-ray flux is often proportional to the soft X-ray flux. This is explained in the canonical solar flare model as follows. The hard X-rays are nonthermal bremsstrahlung radiation produced by the interaction of a flux of accelerated electrons with the ambient atmosphere. The heating of the atmosphere during a flare is provided by the electrons; thus, the hard X-rays effectively measure the flare heating rate. Soft X-rays are produced in the corona, which has been heated during the flare by chromospheric evaporation and direct deposit of nonthermal electron energy flux. The soft X-rays are thermal radiation, measuring the temperature of the corona (and hence the result of the heating). Therefore, the smooth rise in the soft X-ray flux should be proportional to the time integral of the hard X-ray flux.

It is not yet possible to measure the nonthermal hard X-ray emission from stellar flares, so the white-light continuum (which has been observed to trace the hard X-rays during solar flares) is used as a proxy (Hawley et al.

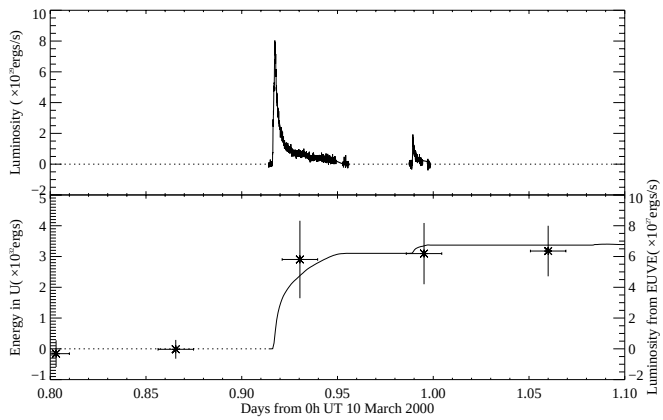

FIG. 4.—*Top*: *U*-band light curve for flares 1 and 2. *Bottom*: *EUVE* light curve (*points*), together with the time-integrated curve for flares 1 and 2 (*solid line*). The left axis of the bottom panel gives the integrated *U*-band energy, while the right axis gives the *EUVE* luminosity. Note that in both panels the quiescent values have been subtracted.

1995). The soft X-rays were measured by *EUVE*. Cully et al. (1997) have calculated the neutral hydrogen column density between AD Leo and the *EUVE* detector to be 3×10^{18} cm^{-2}. Such a small column density means that to a good approximation we can ignore absorption from the interstellar medium.

Our results are shown in Figure 4, where the data have been scaled to stellar surface values. The first panel illustrates the *U*-band photometric light curves for flares 1 and 2, while the second panel shows the cumulative (integrated) *U*-band energy together with the *EUVE* DS light curve spanning this 7 hr period. The rise in the soft X-ray light

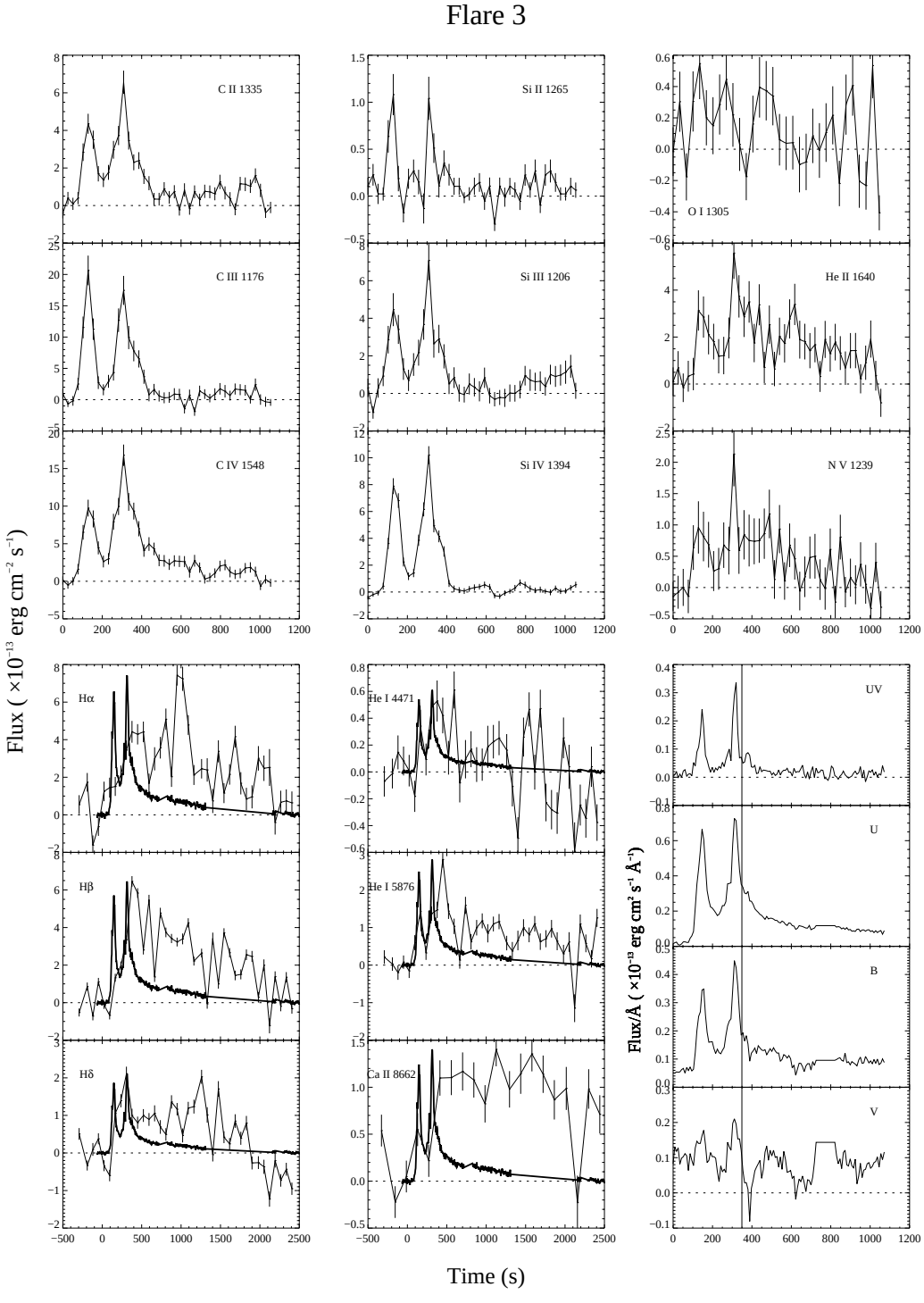

FIG. 5.—Light curves for flare 3. Time is in seconds from the beginning of the flare (5:06:04 UT on 2000 March 11). The vertical axis is the observed flux. The top panels show, from top to bottom, C II, C III, C IV (*left*), Si II, Si III, Si IV (*middle*), and O I, He II, N V (*right*). The bottom left and bottom middle panels show lines measured by the coudé spectrograph. These are, from top to bottom, Hα, Hβ, Hδ (*left*) and He I λ4471, He I λ5876, Ca II λ8662 (*middle*). The bottom right-hand panel shows the continuum light curves in the *UV*, *U*, *B*, and *V* bandpasses. The *U*-band light curve is overplotted in the bottom left and bottom middle panels for reference, as the time axis has been extended to accommodate the long decay times for the optical lines. The vertical line in the continuum light-curve panel marks the beginning of the gradual phase (see § 4.4).

curve is consistent with the Neupert effect, as the peak *U*-band emission coincides with the increase in the DS light curve.

4. LINE AND CONTINUUM EMISSION

Data from three instruments (STIS ultraviolet spectroscopy and McDonald optical spectroscopy and photometry) provided simultaneous continuum and emission line measurements for four flares (3, 6, 7, and 8), while only STIS data were available for flare 4. Figures 5–9 show light curves in several of the strong ultraviolet emission lines (*top panels*) for flares 3, 4, 6, 7, and 8, respectively. Optical emission line (*bottom left and middle panels*) and continuum (*bottom right panels*) light curves are illustrated in Figure 5 (flare 3) and Figures 7–9 (flares 6–8). The optical *U*-band light curve is taken as a fiducial for the identification of the flare impulsive and gradual phases. The transition is determined from the first zero in the derivative of the *U*-band light curve after the flare peak, indicating a change from rapid to slow decay. It is marked by the vertical lines on the continuum light curves in each figure.

4.1. *Continuum Emission*

The primary defining characteristic of stellar flares is a sharp rise in the blue continuum flux. Figures 5–9 clearly illustrate this behavior in the continuum light curves. Figure 10 also shows (for flare 8, but this is true for all of the flares) that the emission peaks in the *U* band, with lower continuum fluxes measured in both the ultraviolet and the red. As discussed in detail in Hawley & Fisher (1992), the only emission mechanism that can fit such a continuum distribution is blackbody emission at a temperature near 10,000 K. Accordingly, we model the flare continuum flux distribution as blackbody emission from the flaring area of the star,

$$F_\lambda = X \frac{R_*^2}{d^2} \pi B_\lambda(T_{\rm fl}) \, , \qquad (1)$$

where X, the fractional flare area coverage, and $T_{\rm fl}$, the blackbody temperature, are free parameters. The radius, R_*, and distance, d, that we used for AD Leo are 3×10^{10} cm (Pettersen 1976) and 1.5×10^{19} cm (Pettersen 1980), respectively. Equation (1) was convolved with the (*UBVR*) filter response functions and then fitted, using weighted least squares, to the measured continuum fluxes as a function of time during each flare. To model the flare-only contribution to the continuum flux, the quiescent flux was subtracted from the total measured flux. Figure 10 shows these fits at four times (A–D, as indicated on Fig. 11) during flare 8. It is clear that a blackbody provides only an approximate fit to the observations and in general does not fit all of the fluxes within the formal errors. However, it does provide the correct overall shape of the continuum and allows us to investigate the possible evolution of the flare temperature and area coverage. Other mechanisms have been tried by several authors, with marginal results (see, e.g., Abranin et al. 1997). A description of the exact nature of the blue continuum emission, as well as the underlying physical mechanism that produces it, remains elusive. We are currently investigating flare continuum emission using new radiative hydrodynamic models of stellar flares (J. C. Allred et al. 2003, in preparation).

Figure 11 illustrates our computed temperature and area coverage for flares 3, 6, 7, and 8 as a function of time. Our results show that each flare has a similar temperature,

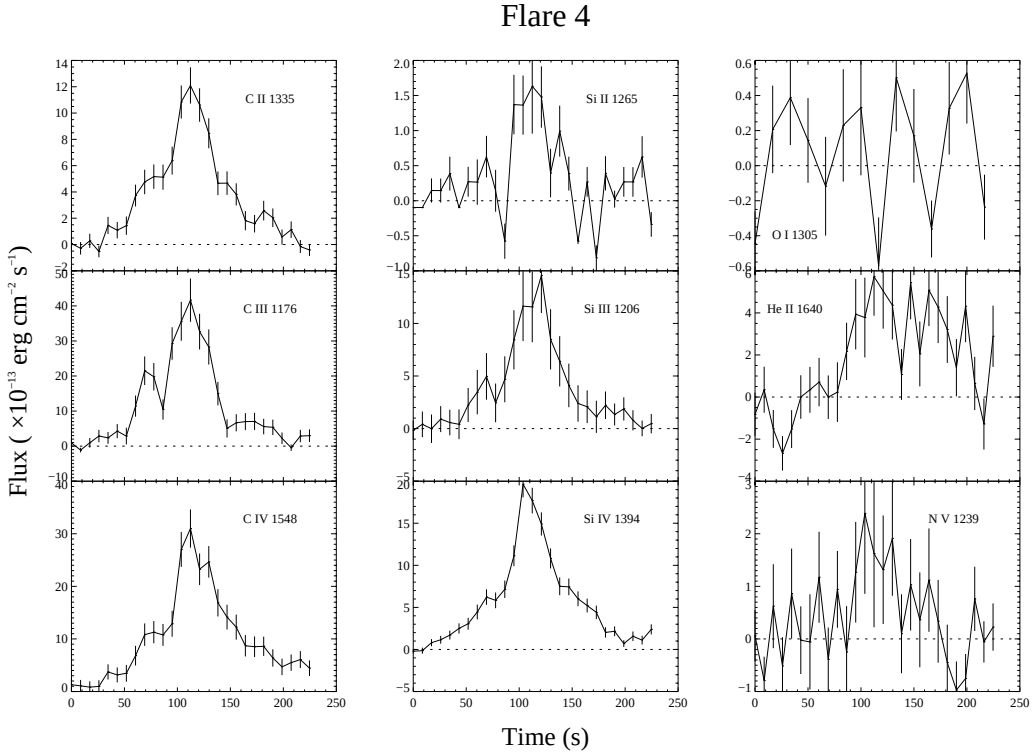

FIG. 6.—Light curves for flare 4. Time is in seconds from 10:12:04 UT on 2000 March 11. The STIS panels correspond to those plotted for flare 3. No optical photometry or coudé data were obtained during this flare.

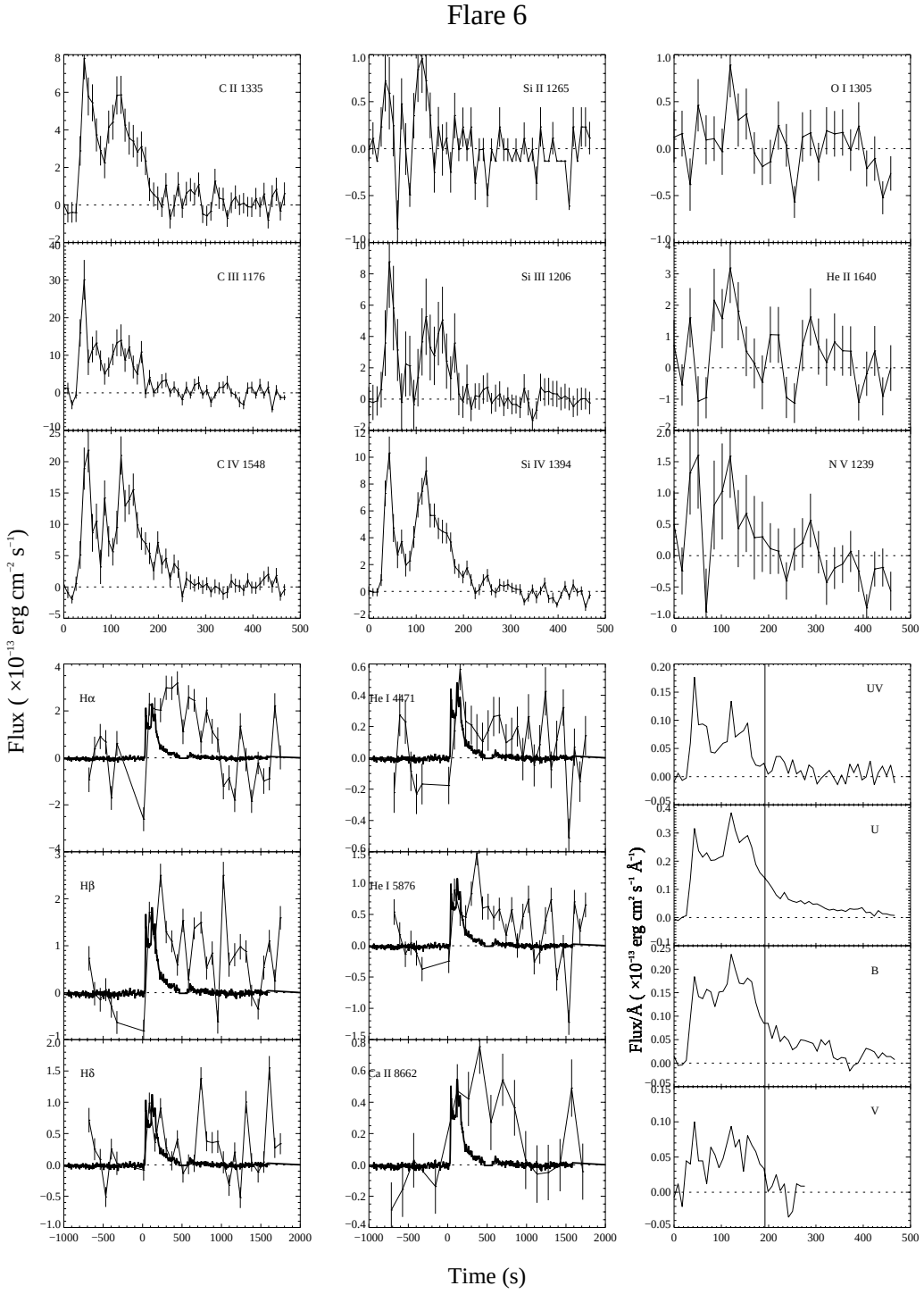

FIG. 7.—Light curves for flare 6. Time is in seconds from 4:03:43 UT on 2000 March 12. The panels correspond to those plotted for flare 3 in Fig. 5.

$T_{\rm fl} \sim 9000$ K, regardless of its duration, peak flux, time evolution, or total energy. It follows that the area coverage must increase with the peak flux (e.g., flare 8 has [8 : 5 : 4] times the area of flares [6 : 7 : 3] at their respective peaks). Note that the inferred areas are small, typically $\sim$0.01% of the visible hemisphere, as expected from the rapid onset and rise of the continuum emission during the impulsive phase. We will show in § 4.4 that the total energy of the flare is correlated primarily with its duration (see Table 4 below), and not with area coverage or temperature. The longest duration flare, flare 7, radiated nearly twice the energy of flare 8, although flare 8 has a much larger peak flux and hence area coverage. These results are in general agreement with those found in Hawley & Fisher (1992).

4.2. *Line Emission*

4.2.1. *Ultraviolet Lines*

Line fluxes were determined for 24 ultraviolet emission lines that were measurably enhanced over their quiescent values during at least one of the flares. The line identifications

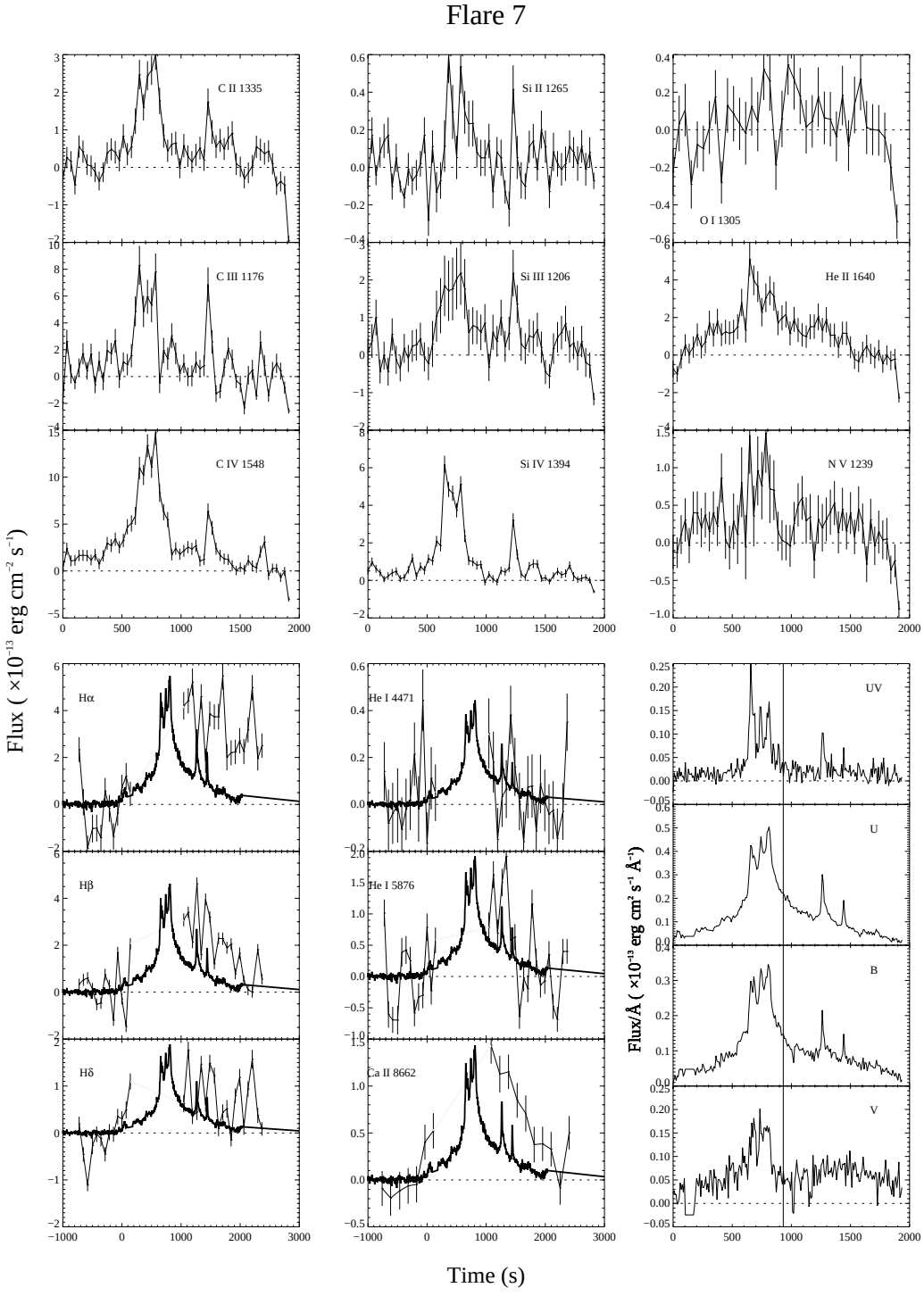

FIG. 8.—Light curves for flare 7. Time is in seconds from 5:21:03 UT on 2000 March 12. The panels correspond to those plotted for flare 3 in Fig. 5.

and formation temperatures (from Dere et al. 1997, 2001), together with the quiescent line fluxes measured from the quiet AD Leo spectrum (see § 2), are listed in Table 2. The line fluxes were computed by integrating the flux, $F_\lambda - F_\lambda^{\rm cont}$, over the line region, where $F_\lambda^{\rm cont}$ is the measured continuum flux in a region adjacent to the line. The quiescent line flux was then subtracted to obtain the flare line flux. By subtracting the full value of the quiescent flux, we have implicitly assumed that the flare area is negligible compared to the quiescent emitting regions. This assumption is justified by our area coverage results in the previous section; however, we note that the area of line emission may be more extensive than the continuum-emitting regions.

Flare-only light curves (quiescent flux has been subtracted) for some representative UV lines (C II, III, and IV; Si II, III, and IV; O I, He II, and N V) are plotted in the upper panels of Figures 5–9. Each panel shows lines in order of increasing ionization stage and hence formation temperature. The UV lines are primarily impulsive, with only He II, C IV, and N V showing extended gradual phases, similar to

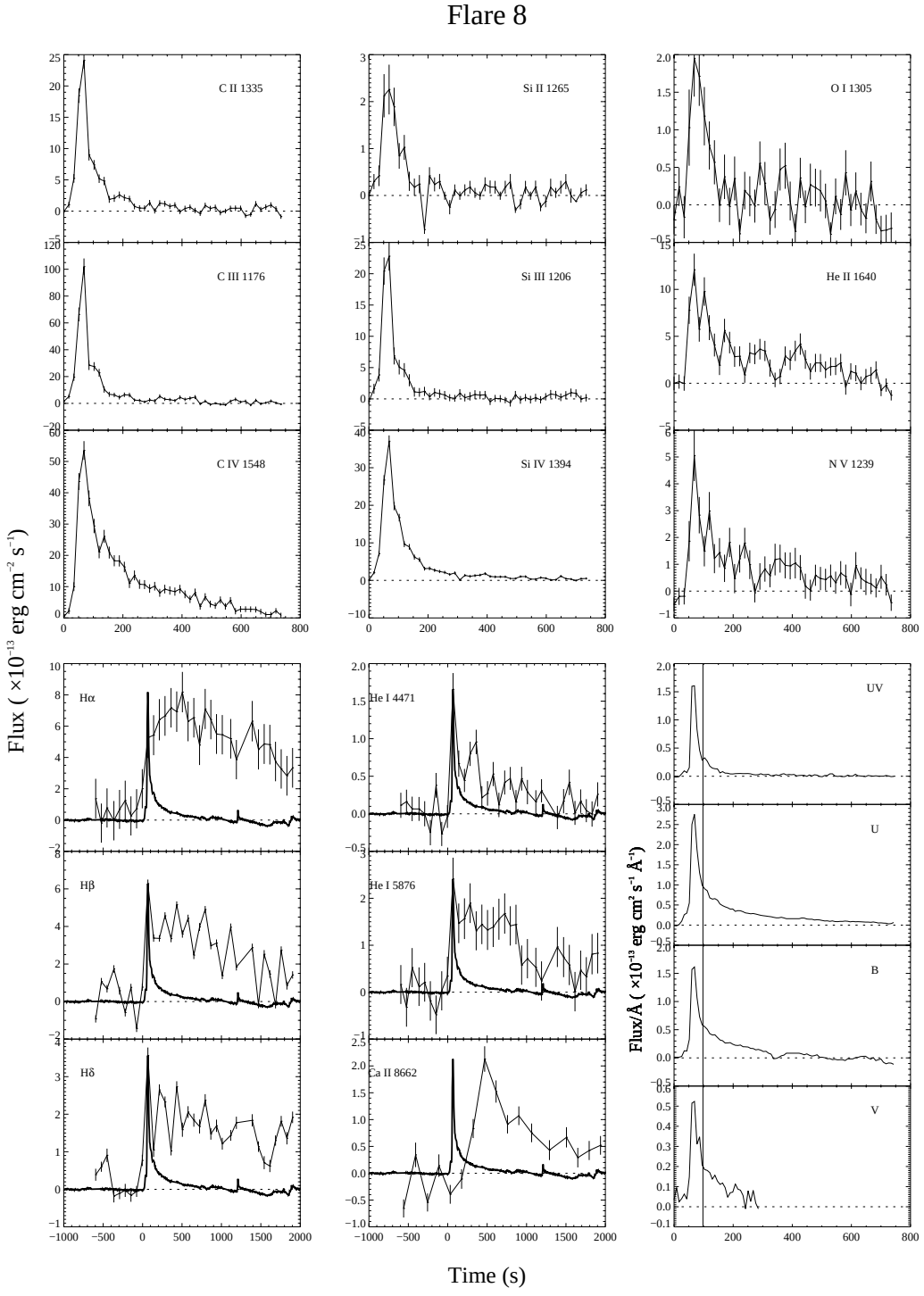

FIG. 9.—Light curves for flare 8. Time is in seconds from 2:29:33 UT on 2000 March 13. The panels correspond to those plotted for flare 3 in Fig. 5.

the *U*-band continuum. Interestingly, the extended gradual phase may be correlated with formation temperature, as C IV and N V are the highest temperature lines measured (other than Fe XXI, which is too weak for quantitative analysis). This would suggest that these lines are formed along with the thermal coronal radiation that marks the gradual phase in solar flares, in agreement with the discussion in Hawley & Fisher (1992). The lower temperature lines fade more quickly, indicating a different atmospheric structure in the transition region during the gradual phase. These data will provide strong constraints on atmospheric models, since they sample many atomic species and many ionization stages of a given species, thus spanning a wide range of formation temperature and atmospheric conditions.

4.2.2. *Optical Lines*

As described in § 2.3, the optical echelle spectra are normalized to unity in each order during the data reduction procedure. To obtain the flux calibration necessary for

TABLE 2
Ultraviolet Emission Lines

Line	log T[a]	F_Q[b]	Comment
C III λ1176	4.8	19.45 ± 0.80	6 lines
Si III λ1206	4.7	13.37 ± 0.74	
N V λ1239[c]	5.3	9.85 ± 0.46	
N V λ1243[c]	5.3	4.91 ± 0.19	
C III λ1247	4.8	0.42 ± 0.14	
Si II λ1265	4.1	1.27 ± 0.09	Doublet
Si III λ1298	4.7	2.29 ± 0.14	4 lines
O I λ1305	<4.0	7.22 ± 0.21	Doublet
Si II λ1309	4.1	0.45 ± 0.06	
Si III λ1313	4.7	0.01 ± 0.04	
C II λ1324	4.4	0.09 ± 0.05	4 lines
C II λ1335	4.4	25.08 ± 0.35	Doublet
Fe XXI λ1354	7.0	0.71 ± 0.07	
Si IV λ1394[c]	4.9	8.51 ± 0.21	
Si IV λ1403[c]	4.9	4.64 ± 0.26	
Si III λ1417	4.7	0.21 ± 0.05	
Si II λ1526	4.1	0.71 ± 0.08	
Si II λ1533	4.1	1.30 ± 0.15	
C IV λ1548[c]	5.0	32.93 ± 0.67	
C IV λ1551[c]	5.0	16.78 ± 0.44	
Fe III λ1560	4.1	5.55 ± 0.24	
He II λ1640	4.7	28.39 ± 0.66	7 lines
C I λ1657	<4.0	15.30 ± 0.54	5–6 lines
Fe II λ1671	4.1	1.27 ± 0.20	

[a] T is the formation temperature of the line.
[b] F_Q is the flux measured in the high-S/N quiescent spectrum, in units of 10^{-14} ergs s^{-1} cm^{-2}.
[c] The two components of the strong N V (λλ1239, 1243), Si IV (λλ1394, 1403), and C IV (λλ1548, 1551) doublets are well resolved in the STIS spectra and were measured separately.

computing absolute line fluxes from these data, we follow a two-step process. First, the spectra were calibrated using spectrophotometric data for AD Leo during quiescence (Pettersen & Hawley 1989). The flare contribution to the continuum flux was then found by interpolating the fluxes measured from the broadband *UBVR* photometry. This method of calibration introduces a systematic uncertainty in the absolute scale of the continuum flux, which we estimate to be less than 10%.

Using the calibrated spectra, we computed line fluxes following the prescription given in § 4.2.1. Optical emission lines that were measured included the first five Balmer lines (Hα through Hε), two of the Ca II IR triplet lines (λλ8498 and 8662), two He I lines (λλ4471 and 5876) and the Ca II H line. The line IDs and quiescent fluxes are given in Table 3. Light curves for Hα, Hβ, Hδ, He I λλ4471 and 5876, and Ca II λ8662 are shown in the bottom left and middle panels of Figures 5–9. Note that these panels have expanded time axes, and the *U*-band light curve is overplotted as a thick solid line to provide a visual benchmark for comparing the data to the continuum and ultraviolet emission lines.

The optical chromospheric emission lines exhibit only a mild impulsive phase but have dramatically stronger and longer gradual phases compared to the ultraviolet lines, in agreement with previous results (Hawley & Pettersen 1991). This is particularly noticeable in flares 3 and 8, which have the best-S/N optical spectra. It does not appear that there is enough energy in the ultraviolet emission lines, nor do they stay elevated long enough, to power these chromospheric lines. The backwarming mechanism suggested by Hawley & Fisher (1992) to provide the energy to produce these lines must therefore come primarily from higher temperature

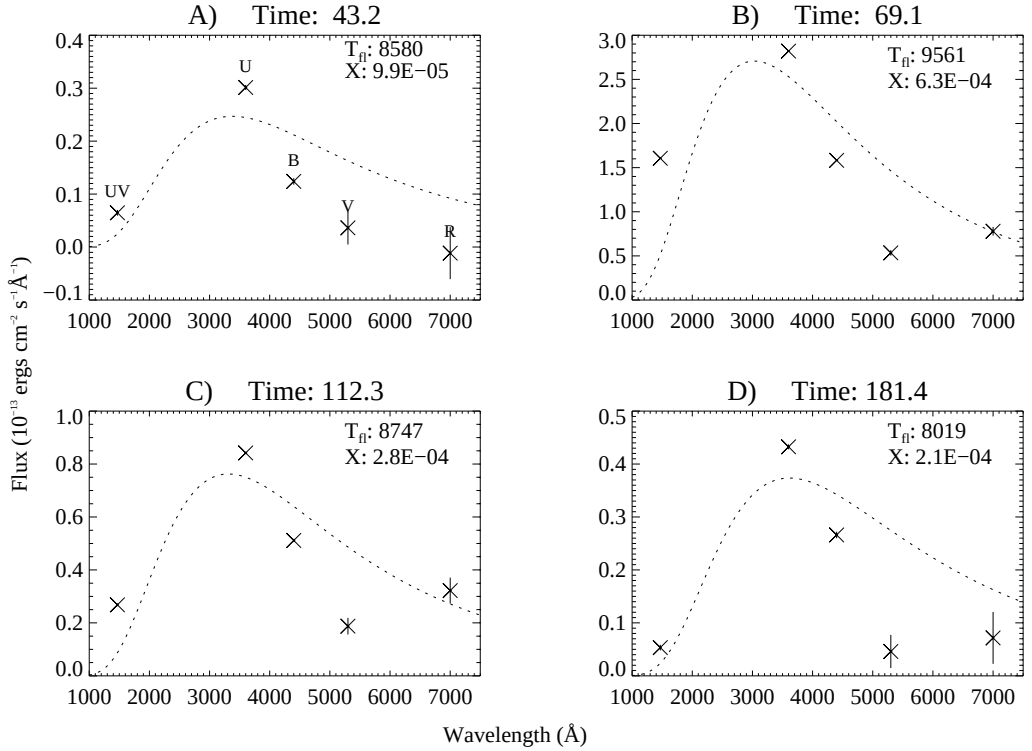

Fig. 10.—Blackbody fits to the optical and UV continua for four times during flare 8. The time indicates the number of seconds since the beginning of the flare (2:29:33 UT 2000 March 13). The observed UV and *U*, *B*, *V*, and *R* measurements are shown as crosses at the central wavelength of each band. The values obtained for the temperature, T_{fl}, and fractional area coverage, X, are indicated in each panel. The letters A–D at the top of each panel indicate the times during the flare evolution when these fits were obtained (see Fig. 11, *bottom right panel*.)

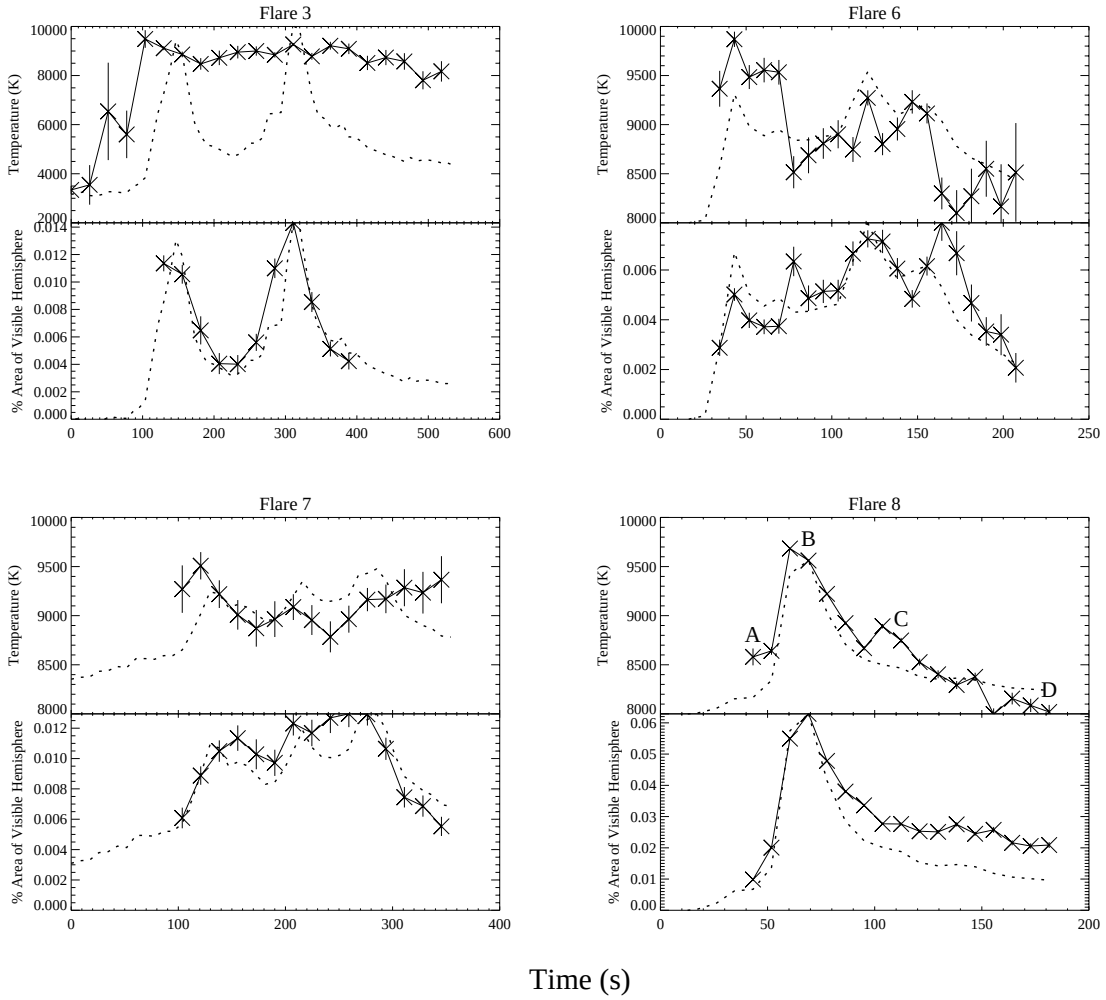

FIG. 11.—Temperature (T_{fl}) and fractional area coverage for flares 3, 6, 7, and 8. The dotted line indicates the *U*-band continuum, which has been scaled to fit on the plots. The time indicates the number of seconds since the beginning of the flare. The labels A–D in the bottom right-hand panel indicate the times when the fits shown in Fig. 10 were obtained.

lines formed in the corona, perhaps including C IV and N V at the coronal/transition region boundary. We still do not have enough data to directly test this hypothesis; the *FUSE* observations were planned to provide those higher temperature diagnostics, but unfortunately, they were not obtained during this flare campaign.

TABLE 3
OPTICAL EMISSION LINES

Line	λ_0[a]	F_Q[b]
Hα	6563	45
Hβ	4861	12
Hγ	4340	5.0
Hδ	4101	3.2
Hϵ	3970	2.0
Ca II	8662	6.6[c]
	8498	4.2[c]
Ca II H	3968	1.2
He I	4471	0.3
He I	5876	0.2

[a] Central wavelength in Å.
[b] F_Q is the flux measured in the quiescent spectrum, in units of 10^{-13} ergs s^{-1} cm^{-2}.
[c] Includes only the central reversal.

We do have indirect evidence that coronal backwarming produces the chromospheric line radiation. The long gradual phase exhibited by the chromospheric lines suggests that they are another manifestation of the Neupert effect, acting in this case as a proxy for the coronal soft X-ray emission. Figure 9 shows that the Hα and *U*-band radiation follow the same Neupert effect behavior as the *U* band and soft X-rays in Figure 4, as expected if this scenario is correct.

4.3. *Line and Continuum Ratios*

Another way to compare the relative timing of the impulsive- and gradual-phase emission is shown in Figure 12, for flare 8. This figure illustrates the ratio of various line fluxes and the UV continuum flux per angstrom to the *U*-band continuum flux per angstrom; the scaled *U*-band light curve is overplotted as the dotted line in each panel. Note that the continuum values are shown as flux per angstrom, since this is a convenient reference for the line fluxes, which are typically integrated over only 1–2 Å. "Flare-only" data are shown on this figure, so occasional negative values of the ratios are spurious and are due to noise in the data. The top

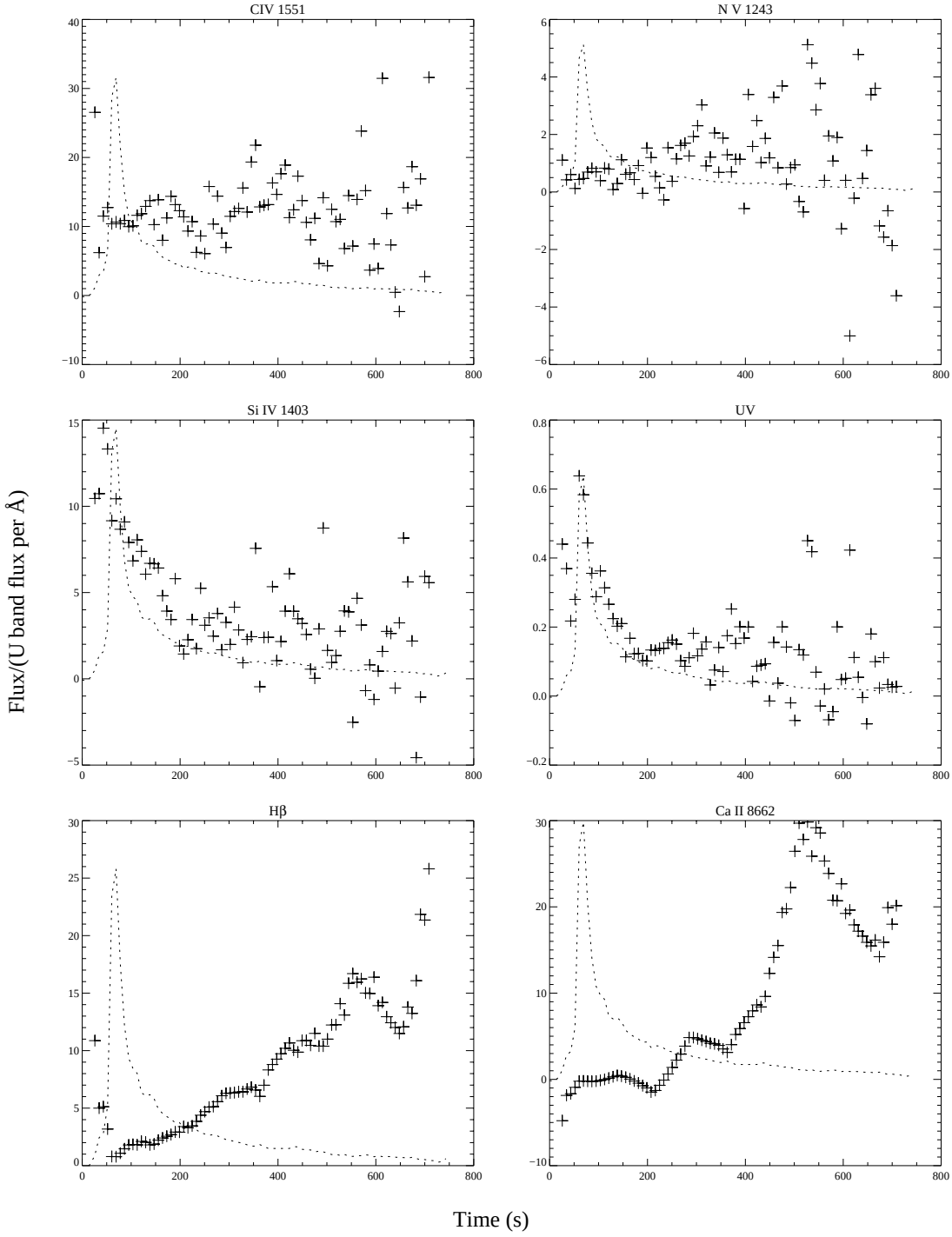

FIG. 12.—Ratios of several line fluxes and the UV continuum flux per angstrom to the flux per angstrom in the *U* band for flare 8. The dotted line stands for the *U*-band light curve scaled to fit on each panel. Time is in seconds from 2:29:33 UT, 2000 March 13. See text for discussion.

panels show that the C IV and N V ratios are essentially flat, indicating that these lines exhibit evolution very similar to that of the *U* band throughout both the impulsive and gradual phases of the flare. The middle panels of Figure 12 show that Si IV and the UV continuum rise much more sharply during the impulsive phase than the *U* band and decay more quickly during the gradual phase. The bottom panels of Figure 12 show that the chromospheric optical lines (Hβ, Ca II λ8662) have little or no impulsive response but grow very strong during the gradual phase (Neupert effect behavior).

The strong correlation between the UV/*U* continuum ratio and the *U*-band light curve is intriguing. The flux-flux plots shown in Figure 13 indicate that the C IV, Si IV, and N V fluxes are well fitted by nearly linear relationships with the *U*-band flux per angstrom. Although the illustrated results are only for flare 8, similar relations hold for flares 3,

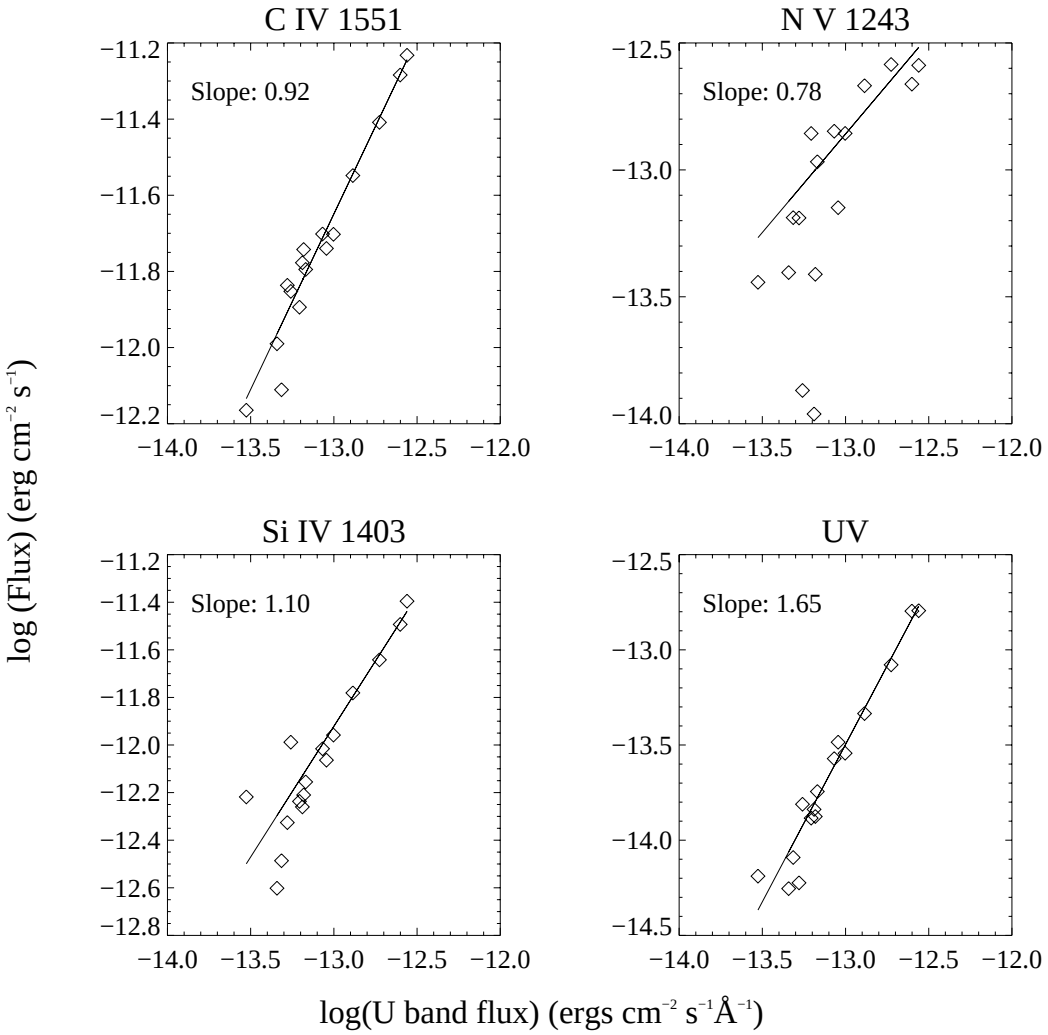

FIG. 13.—*U*-band flux vs. the flux in several line and continuum regions during the impulsive phase of flare 8. Log-log units are used to show the power-law relation between the fluxes plotted. Units are ergs cm^{-2} s^{-1} for all lines and ergs cm^{-2} s^{-1} Å^{-1} for continuum regions.

6, and 7. If the *U*-band continuum were the response of the atmosphere to backheating by UV line emission, the observed linear relationship with UV line fluxes would be expected in an energetic steady state. The UV continuum flux, on the other hand, is proportional to $F_U^{1.7}$, where F_U is the *U*-band flux. The reason for this differing behavior is unexplained as yet; we are investigating these results with our new generation of flare models.

4.4. *Energy Budget*

The flare energy budget comprises the energy emitted in the continuum and from the emission lines listed in Tables 2 and 3. The results are shown in Tables 4–6. The energy contribution due to line emission has been removed from the continuum values. The optical data were interrupted (by clouds) near the end of flare 3, while the *U* and *B* bands were still elevated. Therefore, to estimate the total flare energy for flare 3, we fit the end of the gradual phase to a decaying exponential. This contribution (of approximately 20%) has been included in the values listed for flare 3 in Table 4. Also note that flare 7 had an unusually slow rise during the impulsive phase (see Fig. 8). This has been included in the impulsive portion of the energy budget.

Data for flares 1 and 2 (discussed in § 3) comprise only *U*-band and *EUVE*/DS photometry, so a similar energy budget calculation is not possible. However, we have computed the energies emitted in these two wavelength regimes, with $E_U = 3.4 \times 10^{32}$ ergs and $E_{DS} = 1.1 \times 10^{32}$ ergs for the sum of these two flares. The *U*-band energy is almost an order of magnitude larger than the amount observed in flare 8.

Table 7 summarizes the energy budget results for the flares in which both optical and ultraviolet data were available (3, 6, 7, and 8). These flares have rather different light-curve morphology (recall Figs. 5–9), with flare 7 being the longest and slowest, flare 3 being somewhat more impulsive, flare 6 being a small, mostly impulsive flare, and flare 8 being the most impulsive and also exhibiting the strongest peak flux. Flares 3, 6, and 7 exhibited multiple peaks. Despite these differences, the energy results show that the continuum flux (particularly in the *U* band) carries the vast majority of the energy in all cases, during both the impulsive and gradual phases. Similarly, the ultraviolet emission lines dominate the line emission during all of the impulsive

TABLE 4

CONTINUUM: ENERGY BUDGET

REGION	FLARE 3		FLARE 4		FLARE 6		FLARE 7		FLARE 8	
	0–349 s	349–1072 s	0–173 s	173–223 s	0–192 s	192–468 s	0–828 s	828–1816	0–98 s	98–822 s
Total	46.7	42.6	2.1	0.1	28.4	4.4	139.8	115.2	64.0	61.9
UV continuum	5.6	4.1	5.9	0.4	3.7	0.6	8.0	4.4	9.4	5.7
U[a]	16.7	22.4	...	...	7.6	2.1	31.1	18.8	18.2	28.1
B[a]	12.0	16.1	...	...	6.9	1.7	31.4	20.1	14.4	12.4
V[a]	2.9	0.0	...	...	2.2	0.0	15.7	13.8	5.1	3.5
R[a]	9.6	0.0	...	...	8.0	0.0	53.6	58.2	17.0	12.2
Total	46.7	42.6	5.9	0.4	28.4	4.4	139.8	115.2	64.0	61.9

NOTE.—All values represent the surface flux integrated over time and wavelength for each flare interval, in units of 10^{30} ergs.

[a] Flux contributions from lines within this continuum region have been removed.

TABLE 5

UV EMISSION LINES: ENERGY BUDGET

LINE	FLARE 3		FLARE 4		FLARE 6	FLARE 7		FLARE 8	
	0–349 s	349–1072 s	0–173 s	173–223 s	192–468 s	0–828 s	828–1816 s	0–98 s	98–822 s
C III λ1176	70.3	28.9	69.9	4.9	2.5	53.8	18.3	109.5	71.5
C IV λ1548	57.0	53.7	57.4	8.3	7.5	120.7	42.9	72.8	173.1
C IV λ1551	42.8	29.8	35.6	4.5	6.4	80.9	33.2	55.6	101.5
Si IV λ1394	34.4	11.7	33.8	2.7	1.3	39.7	13.7	45.6	44.7
Si IV λ1403	28.0	7.2	26.0	2.0	1.4	24.1	8.1	35.6	26.2
C II λ1335	23.0	17.6	21.5	1.9	1.6	19.2	9.8	28.4	21.6
Si III λ1206	21.7	13.2	22.3	1.8	0.3	15.1	11.9	27.1	13.8
Si III λ1298	17.9	1.5	17.8	0.6	0.4	9.2	3.9	27.1	8.6
He II λ1640	16.8	35.8	9.4	3.4	1.5	44.5	23.4	12.7	43.8
Fe II λ1671	6.9	7.2	0.0	0.2	0.0	15.1	0.0	2.5	0.0
N V λ1239	5.2	8.0	3.2	0.0	0.0	10.7	5.3	4.4	14.8
C III λ1247	4.0	2.0	2.6	0.3	0.1	1.8	1.1	7.1	1.4
Fe III λ1560	3.7	3.1	0.3	0.2	1.1	1.4	1.0	0.9	4.4
Si II λ1265	2.9	2.1	1.9	0.0	0.0	2.2	1.1	3.4	2.5
N V λ1243	2.4	5.8	1.9	0.5	0.0	5.0	1.7	2.6	8.4
C I λ1657	2.3	6.3	3.0	0.7	0.7	4.4	6.4	3.2	4.0
O I λ1305	2.2	2.0	0.3	0.1	0.0	0.3	2.1	2.2	2.9
C II λ1324	2.0	0.9	1.1	0.1	0.0	1.4	0.6	1.9	1.5
Si III λ1417	1.6	0.6	1.4	0.0	0.0	1.5	0.3	2.8	0.5
Si II λ1533	1.6	0.0	0.1	0.4	0.0	0.7	0.0	2.2	1.4
Si II λ1309	1.6	0.9	1.4	0.0	0.1	0.5	0.8	1.6	1.3
Si III λ1313	1.5	0.2	0.7	0.1	0.1	0.1	0.4	2.5	0.4
Si II λ1526	1.1	1.2	1.2	0.0	0.4	0.6	1.1	2.2	1.1
Fe XXI λ1354	0.5	0.0	0.0	0.0	0.2	0.2	0.4	0.4	1.3
Total	351.2	239.4	305.2	29.6	23.5	453.0	183.9	454.4	544.0

NOTE.—All values represent the surface flux integrated over time and wavelength for each flare interval, in units of 10^{28} ergs.

TABLE 6

OPTICAL EMISSION LINES: ENERGY BUDGET

Line	FLARE 3		FLARE 6		FLARE 7		FLARE 8	
	0–349 s	349–3070 s	0–192 s	192–2100 s	0–828 s	828–3890 s	0–98 s	98–3600 s
Hα	2.7	17.2	0.8	3.2	2.5	19.7	2.5	35.0
Hβ	2.4	13.7	0.8	3.3	6.1	7.6	1.8	25.1
Hγ	0.7	2.2	0.7	0.9	1.1	3.4	1.0	17.7
Hδ	1.1	3.6	0.5	1.3	3.2	4.9	1.0	16.1
Hε	1.1	2.2	0.0	2.5	3.6	5.7	0.6	6.5
Ca II λ8662	0.5	6.8	0.3	1.8	2.0	2.2	0.0	10.2
Ca II λ8498	0.3	8.0	0.0	1.2	0.0	1.7	0.0	4.5
Ca II H	0.3	0.6	0.0	0.6	0.3	0.1	0.3	3.2
He I λ4471	0.7	3.8	0.3	1.6	3.6	2.8	0.6	4.1
He I λ5876	1.1	5.0	0.0	1.4	1.7	1.4	0.7	5.7
Total	10.7	54.5	2.7	17.7	24.0	49.4	7.7	128.0

NOTE.—All values represent the surface flux integrated over time and wavelength for each flare interval, in units of 10^{29} ergs.

TABLE 7
TOTAL ENERGY

REGION	FLARE 3		FLARE 6		FLARE 7		FLARE 8	
	Impulsive	Gradual	Impulsive	Gradual	Impulsive	Gradual	Impulsive	Gradual
Continuum	466.8 (0.91)[a]	425.5 (0.84)	284.3 (0.92)	43.9 (0.69)	1398.1 (0.95)	1152.2 (0.94)	640.5 (0.92)	618.7 (0.77)
UV lines	35.1 (0.07)	23.9 (0.05)	23.4 (0.08)	2.3 (0.04)	45.3 (0.03)	18.4 (0.02)	45.4 (0.07)	54.4 (0.07)
Optical lines	10.7 (0.02)	54.5 (0.11)	2.7 (0.01)	17.7 (0.28)	24.0 (0.02)	49.4 (0.04)	7.7 (0.01)	128.0 (0.16)
Total	512.7	504.0	310.3	64.0	1467.4	1220.1	693.6	801.0

NOTE.—All values represent the surface flux integrated over time and wavelength for each flare interval, in units of 10^{29} ergs.
[a] Numbers in parentheses indicate the ratio of the region's energy to the total energy during that phase of the flare.

phases, while the optical lines dominate the line emission during all of the gradual phases. The relative ratios of [UV lines : optical lines : continuum] are also similar, at [0.07 : 0.02 : 1] during the impulsive phases and [0.05 : 0.18 : 1] during the gradual phases. The optical results agree with those of Hawley & Pettersen (1991), while the ultraviolet results represent a new diagnostic that has not previously been measured.

The astonishing similarity between flares in the numerous atmospheric emission diagnostics, despite the large disparity in the detailed flare evolution for this sample of flares, suggests a common mechanism for flare heating and energy deposition. The flare atmospheres apparently have similar temperature and density structure and hence emission properties over the temperature range 5×10^3 to 5×10^5 K. Indeed, the optical continuum results for many flares on a variety of stars, which show that temperatures of $\sim$9000 K are ubiquitous, suggest that this may be true for stellar flares in general. More data are necessary to confirm these trends, especially in the higher energy (extreme-ultraviolet and X-ray) regimes that map the corona.

The measured optical and ultraviolet flare luminosity, L_f, may be computed for each phase of each flare from the energies (Table 7) and durations (Table 5). These range from 0.2×10^{29} ergs s^{-1} for the gradual phase of flare 6 to 7.1×10^{29} ergs s^{-1} for the impulsive phase of flare 8. The bolometric luminosity of an M3 star such as AD Leo is $\sim 5.9 \times 10^{31}$ ergs s^{-1}; hence, the ratio $L_f/L_{\rm bol}$ ranges from 3×10^{-4} to 1×10^{-2} for the flares observed here. By comparison, the quiescent magnetic activity on AD Leo gives rise to X-ray luminosity at the level $L_{\rm X}/L_{\rm bol} = 9 \times 10^{-4}$ (Giampapa et al. 1996) and Hα luminosity $L_{\rm H\alpha}/L_{\rm bol} = 2 \times 10^{-4}$ (Hawley, Gizis, & Reid 1996).

4.5. *Line Broadening*

Figure 14 shows the line broadening at the base of the strong hydrogen Balmer lines and He I λ5876 for flares 3 and 8 (the only ones in which measurements were possible). The full width at one-tenth of the maximum value is used as a fiducial, as measured by double-Gaussian fits to the observed line profiles. The increased line widths of the Balmer lines may be due to the Stark effect from the increased electron density in the flaring atmosphere (Donati-Falchi et al. 1985; Johns-Krull et al. 1997). The flares we observed were evidently not strong enough to cause the significant broadening (up to 30 Å) seen in previous flares on AD Leo (Hawley & Pettersen 1991). The present data indicate that some broadening has occurred but are insufficient to place strong constraints on the electron density.

Other possibilities are (1) that the weak broadening seen in the present data is due to curve of growth effects in the line wings as the core becomes optically thick, and (2) that the broadening is due to mass motions (see, eg., Eason et al. 1992). We hope to distinguish between these effects with our new generation of flare models.

To investigate mass motions, we have examined the Hα profiles during flare 8 using the flux-weighted line-center method described in the next section. The data are noisy and have relatively poor time resolution, so the full analysis carried out on the ultraviolet lines is not possible. However, we do find that there is an indication of a blueshift of $\sim$40 km s^{-1} during the impulsive phase. This is of the same magnitude, but in the opposite sense (upflow), as the results for the transition region lines. Clearly, Hα data with better time resolution (on larger flares!) would be desirable to investigate these effects in more detail.

4.6. *Velocity Fields*

The strongest ultraviolet lines had enough signal during flares 3 and 8 that we were able to extract spectra with high time resolution and examine changes in the velocity of the atmosphere in the line formation region. The lines exhibit significant redshifts, corresponding to a net downward flow of material in this part of the atmosphere.

We measured the velocities using two different methods. The first method consisted of simply calculating the flux-weighted line center from the line profile data. The second method employed a double-Gaussian fit to the measured line profile, with one Gaussian fixed at the nominal line-center position, and the other Gaussian allowed to move in redshift to best fit the profile. Unfortunately, the majority of the data were too noisy to obtain good Gaussian fits, so the results reported here are from the flux-weighted line-center method.

Figure 15 shows the velocity evolution of C IV λ1548 and Si IV λ1403 during flares 3 and 8. The appearance of large redshifts in UV lines, during and after the flare impulsive phase, is analogous to the "chromospheric condensation" behavior seen in solar flares. Fisher (1989) showed that the peak downflow speed is related to the flare energy during chromospheric evaporation by

$$v_{\rm peak} \simeq 0.4 \left(\frac{F_{\rm evap}}{m n_{\rm ch}} \right)^{1/3}, \qquad (2)$$

where $F_{\rm evap}$ is the total flare energy flux at the peak of the flare and $m n_{\rm ch} = \rho$ is the chromospheric density.

We compare our results to this model as follows. We estimate $F_{\rm evap}$ by totaling the flux in the *UBVR* filters,

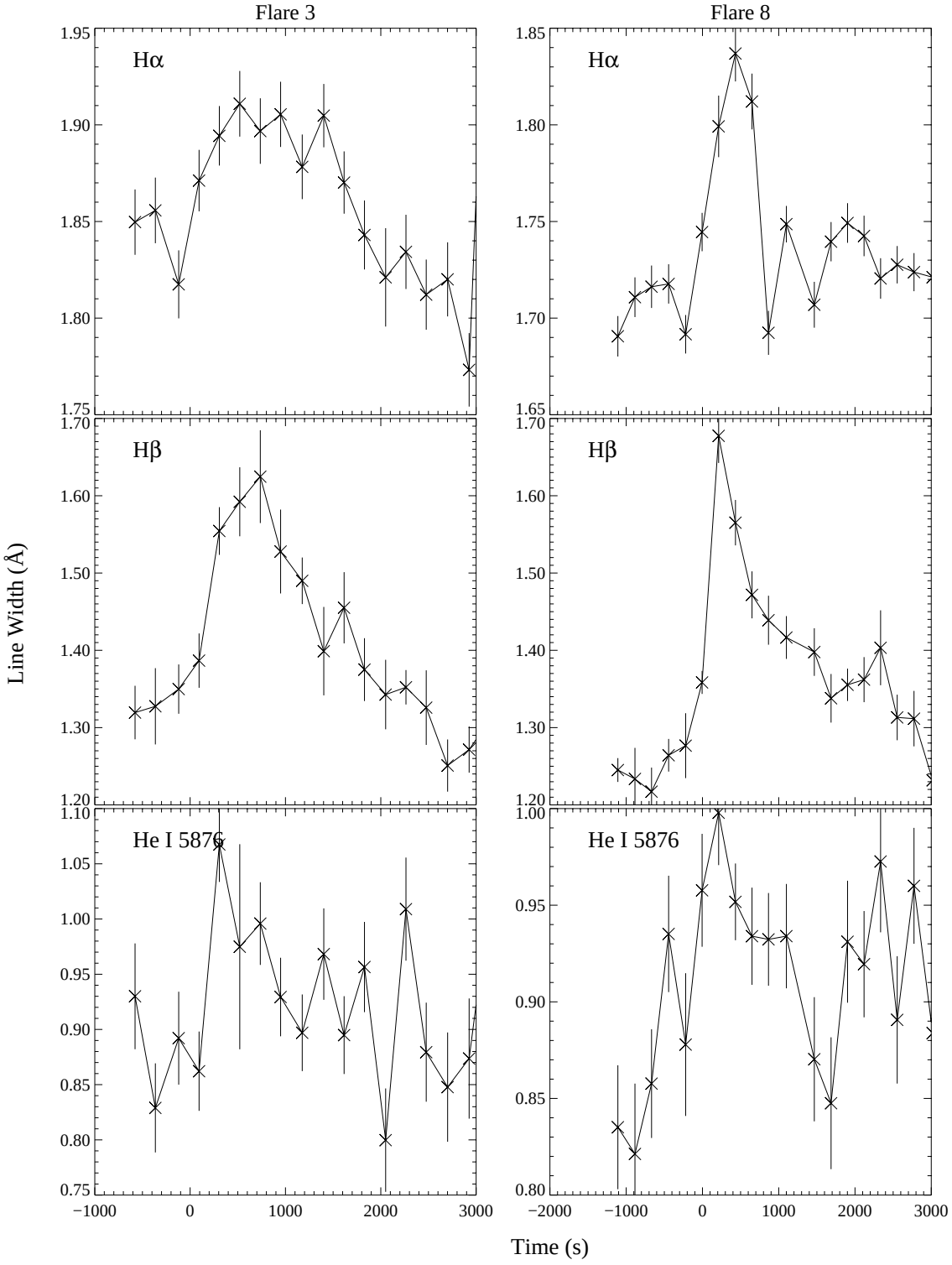

FIG. 14.—Full widths at 0.1 maximum for Hα, Hβ, and He I λ5876 during flares 3 and 8

converting to surface flux, and dividing by the fractional area coverage computed in § 4.1. For flare 8 we find $F_{\rm evap} = 1.6 \times 10^{11}$ ergs cm^{-2} s^{-1}. Using a chromospheric density of 1.5×10^{-10} g cm^{-3} (model B of Mauas & Falchi 1996) results in a peak speed of $\sim$41 km s^{-1}. The observed peak velocities of $\sim$30–40 km s^{-1} are therefore slightly lower then the value predicted with the chromospheric condensation model. The consistently lower measured values may be an artifact of the flux-weighted line center for calculating the velocities. This method essentially averages the quiescent and flare flux leading to systematically smaller velocities. The Gaussian fit method attempts to account for the quiescent flux independently, and the few profiles for which we were able to obtain good fits did show larger velocities

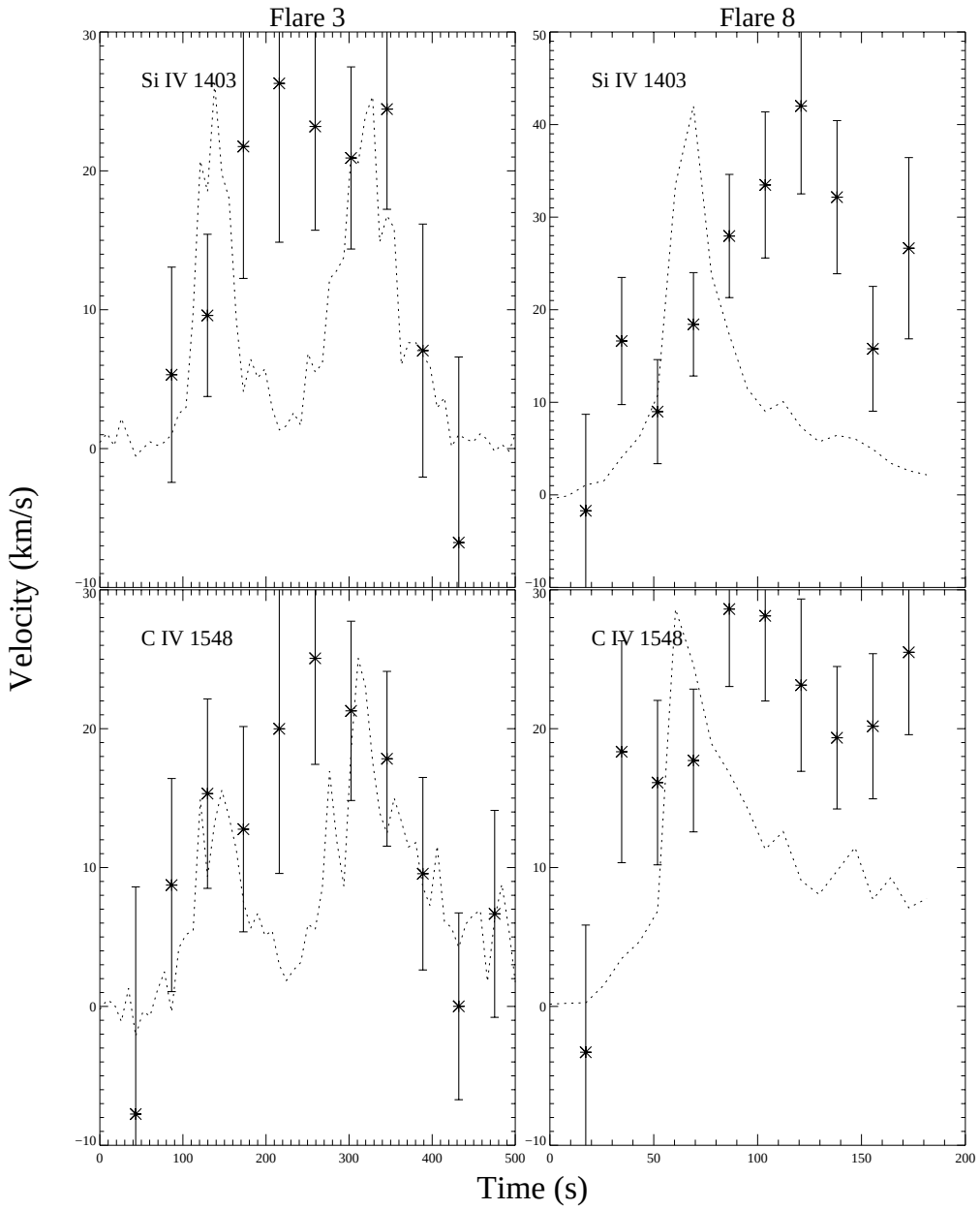

FIG. 15.—Average velocities (*points*) and, for reference, corresponding light curves (*dotted lines*) for Si IV λ1403 and C IV λ1548 during flares 3 and 8

compared to those from the flux-weighted line-center method. Thus, it appears that the chromospheric condensation model provides a reasonable explanation for our velocity data.

5. SUMMARY

We have presented observations and analysis of a large body of flare data obtained during a multiwavelength observing campaign on the dM3e star AD Leo during 2000 March. The combination of *EUVE* soft X-ray and *HST*/STIS ultraviolet observations, together with optical photometry and spectroscopy, provides unprecedented diagnostics of the simultaneous response of many regions of the flare atmosphere. Our results confirm previous work indicating that stellar flares exhibit a Neupert effect in both soft X-rays and chromospheric emission, when compared to the *U*-band continuum radiation. Further, the optical and ultraviolet line and continuum radiation exhibits remarkable correlations that hold for flares of dissimilar light-curve morphology and evolution. These results suggest that the flare-heating mechanism and resulting atmospheric structure are relatively independent of the exact timing and magnitude of the flare energy deposition. In all cases, a flare continuum temperature of ~9000 K is indicated, with small area coverage (<0.1%). The optical continuum carries the bulk of the energy, with the ultraviolet lines contributing a few percent during the impulsive phase, while the optical lines contribute ~10%–20% during the gradual phase. The high-resolution spectroscopic observations of strong

ultraviolet lines allowed us to determine the velocity evolution of the strongest flares we observed. The data show significant downflows, in agreement with chromospheric condensation models for solar flares.

The wealth of observational data presented here places strong constraints on models of flare energy deposition and heating in stellar flare atmospheres. We are now adapting a radiative hydrodynamic code (Carlsson & Stein 1997; Abbett & Hawley 1999) for use in modeling the AD Leo atmosphere, with the ultimate goal of understanding the heating of the lower atmosphere and production of the white-light continuum radiation.

This research was made possible by grant HST-GO-8613 from the Space Telescope Science Institute, operated by the Association of Universities for Research in Astronomy, Inc., for NASA. We wish to thank the Kavli Institute for Theoretical Physics at the University of California, Santa Barbara, for their support through their program on Solar Magnetism and Related Astrophysics, and for their hospitality during the visits of S. L. Hawley, C. M. Johns-Krull, G. H. Fisher, W. P. Abbett, and J. C. Allred to the KITP during the spring of 2002. Our thanks also go to the support staff at the McDonald Observatory, University of Texas, Austin for assisting with the flare campaign. S. L. Hawley and G. H. Fisher were funded in part through a Guest Investigator grant awarded through the NASA *FUSE* GI program.

REFERENCES

Abbett, W. P., & Hawley, S. L. 1999, ApJ, 521, 906
Abranin, E. P., et al. 1997, Ap&SS, 257, 131
Bookbinder, J. A., Walter, F. M., & Brown, A. 1992, in ASP Conf. Ser. 26, Cool Stars, Stellar Systems, and the Sun, ed. M. S. Giampapa & J. A. Bookbinder (San Francisco: ASP), 27
Carlsson, M., & Stein, R. F. 1997, ApJ, 481, 500
Cully, S. L., Fisher, G. H., Hawley, S. L., & Simon, T. 1997, ApJ, 491, 910
Dennis, B. R., & Zarro, D. M. 1993, Sol. Phys., 146, 177
Dere, K. P., Landi, E., Mason, H. E., Monsignori Fossi, B. C., & Young, P. R. 1997, A&AS, 125, 149
Dere, K. P., Landi, E., Young, P. R., & Del Zanna, G. 2001, ApJS, 134, 331
Donati-Falchi, A., Falciani, R., & Smaldone, L. A. 1985, A&A, 152, 165
Eason, E. L. E., Giampapa, M. S., Radick, R. R., Worden, S. P., & Hege, E. K. 1992, AJ, 104, 1161
Fisher, G. H. 1989, ApJ, 346, 1019
Giampapa, M. S., Rosner, R., Kashyap, V., Fleming, T. A., Schmitt, J. H. M. M., & Bookbinder, J. A. 1996, ApJ, 463, 707
Güdel, M., Benz, A. O., Schmitt, J. H. M. M., & Skinner, S. L. 1996, ApJ, 471, 1002
Hawley, S. L., & Fisher, G. H. 1992, ApJS, 81, 885
Hawley, S. L., Gizis, J. E., & Reid, I. N. 1996, AJ, 112, 2799
Hawley, S. L., & Pettersen, B. R. 1991, ApJ, 378, 725
Hawley, S. L., et al. 1995, ApJ, 453, 464
Herbig, G. H. 1956, PASP, 68, 531
Hinkle, K., Wallace, L., Valenti, J. A., & Harmer, D., ed. 2000, Visible and Near-Infrared Atlas of the Arcturus Spectrum 3727–9300 A (San Fransisco: ASP)
Hurwitz, M., Sirk, M., Bowyer, S., & Ko, Y. 1997, ApJ, 477, 390
Johns-Krull, C. M., Hawley, S. L., Basri, G., & Valenti, J. A. 1997, ApJS, 112, 221
Joy, A. H., & Humason, M. L. 1949, PASP, 61, 133
Landolt, A. U. 1973, AJ, 78, 959
———. 1992, AJ, 104, 340
Liebert, J., Kirkpatrick, J. D., Reid, I. N., & Fisher, M. D. 1999, ApJ, 519, 345
Malina, R. F., & Bowyer, S. 1991, in Extreme Ultraviolet Astronomy, ed. R. F. Malina & S. Bowyer (New York: Pergamon), 397
Mauas, P. J. D., & Falchi, A. 1996, A&A, 310, 245
Mavridis, L. N., Asteriadis, G., & Mahmoud, F. 1982, in Compendium in Astronomy, ed. E. G. Mariolopoulos, P. S. Theocaris, & L. N. Mavridis (Dordrecht: Reidel), 253
McTiernan, J. M., Fisher, G. H., & Li, P. 1999, ApJ, 514, 472
Pettersen, B. R. 1976, Inst. Theor. Astrophys. Blindern Oslo Rep., 46, 1
———. 1980, A&A, 82, 53
Pettersen, B. R., & Hawley, S. L. 1989, A&A, 217, 187
Pettersen, B. R., et al. 1990, in IAU Symp. 137, Flare Stars in Star Clusters, Associations, and the Solar Vicinity, ed. L V. Mirzoyan, B. R. Pettersen, & M. K. Tsvetkov (Dordrecht: Kluwer), 15
Piskunov, N. E., & Valenti, J. A. 2002, A&A, 385, 1095
Rodono, M., et al. 1989, in IAU Colloq. 104, Solar and Stellar Flares, ed. B. M. Haisch & M. Rodono (Cambridge: Cambridge Univ. Press), 53
Siegmund, O. H. W., Lampton, M., Chakrabarti, S., Vallerga, J., & Bowyer, S. 1986, Proc. SPIE, 627, 660
Sirk, M. M., Vallerga, J. V., Finley, D. S., Jelinsky, P., & Malina, R. F. 1997, ApJS, 110, 347
Tull, R. G., MacQueen, P. J., Sneden, C., & Lambert, D. L. 1995, PASP, 107, 251